

**THE EFFECT OF TOOL EDGE RADIUS ON CUTTING CONDITIONS BASED
ON UPDATED LAGRANGIAN FORMULATION IN FINITE ELEMENT
METHOD**

**THE EFFECT OF TOOL EDGE RADIUS ON CUTTING CONDITIONS BASED
ON UPDATED LAGRANGIAN FORMULATION IN FINITE ELEMENT
METHOD**

By

ARDALAN EMAMIAN

B. Eng., (Islamic Azad University of Khomeinishahr, Iran)

A Thesis

Submitted to the School of Graduate Studies

in Partial Fulfilment of the Requirements

for the Degree

Master of Applied Science

McMaster University

© Copyright by Ardalan Emamian, December, 2017

MASTER OF APPLIED SCIENCE (2017)

McMaster University

(Mechanical Engineering)

Hamilton, Ontario

**TITLE: THE EFFECT OF TOOL EDGE RADIUS ON CUTTING CONDITIONS
BASED ON UPDATED LAGRANGIAN FORMULATION IN FINITE ELEMENT
METHOD**

AUTHOR: Ardalan Emamian, B. Eng., (Islamic Azad University of Khomeinishahr, Iran)

SUPERVISORS:

Dr. Stephen C. Veldhuis

Dr. Eugene Ng

Department of Mechanical Engineering

McMaster University

NUMBER OF PAGES:

xix, 104

Abstract

Tool wear is a significant problem for manufacturing companies and represents a major challenge in their operations, but it is also a way they can gain a competitive advantage. To do this it is important to set up a standard procedure to develop high performing tooling. This thesis outlines how the Finite Element (FE) method can be used to understand and develop tool geometry. FE based simulation, as a numerical method, is a reliable method to assess the performance of a cutting tool before conducting machining tests based on the force and temperature profile predicted by the FE model. Defining a mathematical model which can be used as a built-in algorithm for tool wear prediction is very challenging and time consuming. Instead there is a possibility of using other factors such as stress distribution and temperature profile and correlate them to tool wear. In this research, the performance of different tool edge radius in cutting has been studied through experiments and in parallel Updated Lagrangian Models have been developed through ABAQUS/EXPLICIT for various cutting conditions, and experimental data was used to validate the data that has been generated from the finite element models. These models are very convenient to develop and capable of being applied for other types of material and cutting conditions. Thus, they represent an efficient way to reduce the amount of experiments needed to improve a tooling, the machining process, and thereby provide an effective way to increase the machining productivity of manufacturing companies.

Acknowledgements

I would like to express my grant gratitude to my supervisors Dr. Stephen Veldhuis and Dr. Eugene Ng who supported me with their patience, immense knowledge and compassion to carry out this research. I was so fortunate to have supervisors who are knowledgeable in the area of machining and simulation. Their insightful suggestions and their unique solutions for complicated problems contributed greatly to my research.

Also I would like to thank Dr. Maryam Aramesh, Postdoctoral research engineer in the McMaster Manufacturing Research Institute (MMRI). She helped me with her experience and strong background in machining. She has been very approachable and patient whenever I had any questions. I was also very lucky to work in the MMRI where I had an opportunity to experience working with different CNC machines, cooperating with companies and trying to solve their problems by design modification, doing lab scale experiments or even, making some parts on CNC machines. Moreover, I found the MMRI to be one of the most organized labs with a friendly atmosphere. Reflecting back I had many great experiences working with students, researchers and Postdocs who I learnt a lot from. I would like to thank everyone who helped me in this journey.

Last but not least, I am extremely grateful to my parents, my brothers and their families who encouraged me and helped me to feel positive whenever I faced any problem during my research. My special thanks is to my brother Dr. Ali Emamian who I am gratefully indebted to his support and compassion with his insightful advises, selfless help, support and his continuous encouragement from the first day that I came to Canada.

Table of Contents

Abstract.....	iii
Acknowledgements.....	iv
Table of Contents.....	v
List of Figures.....	ix
List of Tables.....	xiii
List of all Abbreviations and Symbols.....	xiv
1. Introduction.....	1
1.1 Research objectives.....	2
2. Literature Review.....	2
2.1 Mechanics of material removal.....	2
2.2 Oblique cutting vs. orthogonal Cutting.....	4
2.3 Analytical Models:.....	6
2.3.1 Merchant Model.....	6
2.3.2 Lee and Shaffer.....	9
2.4 Chip formation.....	11
2.5 Temperature in machining.....	16
2.6 Cutting Edge Geometry.....	22
2.6.1 Chamfered Tools.....	29
2.6.2 Honed tools.....	30

2.6.3	VMG cutting inserts	33
2.7	Tool Wear.....	35
2.7.1	Flank Wear	37
2.7.2	Crater wear	38
2.8	Tool wear Mechanisms	39
2.8.1	Adhesion	40
2.8.2	Abrasion	40
2.8.3	Diffusion	40
2.8.4	Oxidation.....	41
2.8.5	Fatigue.....	41
2.8.6	Plastic Deformation.....	41
2.9	Edge Preparation.....	42
2.10	Friction in machining.....	44
2.11	Coating	46
2.11.1	CVD Coating	48
2.11.2	PVD Coating.....	49
2.12	Stress flow	50
2.13	Damage Models	50
2.14	Failure Criteria Models.....	53

2.14.1	Element Failure Criteria	53
2.14.2	Meshless Methods	55
3.	Modeling	55
3.1	Modeling Formulations	56
3.1.1	Lagrangian	56
3.1.2	Eulerian	57
3.1.3	Arbitrary Lagrangian Eulerian (ALE)	57
3.2	Methodology	58
3.3	Element Definition	59
3.4	Material Model	60
3.5	Boundary conditions	63
4.	Experimental Work	65
4.1	Edge radius measurement by ALICONA	71
5.	Results and Discussion	73
5.1	Tool wear	73
5.2	Cutting forces	80
5.3	Force data analysis	81
5.4	Temperature	84
5.5	Equivalent Plastic Strain (PEEQ)	92
6.	Conclusions	93

7. Recommendations for Future Work.....	94
8. References.....	96

List of Figures

Fig 1) Shear plane for a) sharp tool, b) Rounded tool tip	3
Fig 2) Deformation zones in metal cutting	4
Fig 3) a) Orthogonal Cutting b) Oblique cutting	5
Fig 4) Chip free diagram.....	6
Fig 5) Merchant Circle.....	7
Fig 6) Lee and Shaffer shear model based on Mohr's circle	10
Fig 7) Proof of Lee and Shaffer	10
Fig 8) chip types, a) continuous chip b) Discontinuous chip c) Saw-tooth chip d) Continuous with BUE.....	12
Fig 9) Hard to break chips generated from AISI 1045.....	13
Fig 10) chip formation by using chip breaker [11]	14
Fig 11) non-breakable chips in the left side vs. chip jamming in the right side in same operation	15
Fig 12) Quick stop device [12]	16
Fig 13)Temperature profile captured by infrared camera [12] vs. FEA	18
Fig 14) Heat dissipation percentage to tool, workpiece and chip [8].....	18
Fig 15) Different types of single point turning inserts.....	23
Fig 16) Definition of tool angles.....	24
Fig 17) Macroscopic and Microscopic features of a cutting insert [19]	25
Fig 18) Chamfer geometry characterization [19].....	26
Fig 19) Worn tool surface irregularities.....	26
Fig 20) K- factor method for cutting edge characterization [19]	27
Fig 21) Uhlmann method for edge radius characterization [19]	28
Fig 22) The effect of chamfer angle on cutting forces [24]	30

Fig 23) Stagnation point distance for a) R75 b) R100 [25].....	32
Fig 24) different zones of the chip root.....	33
Fig 25) Comparison between conventional microgeometry and variable microgeometry [31].....	34
Fig 26) Temperature distribution for uniform and variable microgeometry tool [31].....	35
Fig 27) Pin and disk friction test by Burwell and Strang [32]	36
Fig 28) Tool wear curve regions	37
Fig 29) Flank wear vs. crater wear.....	38
Fig 30) Crater wear	39
Fig 31) tool wear mechanisms vs temperature and cutting speed [33]	39
Fig 32) Plastic deformation and edge chipping [Sandvik].....	42
Fig 33) Sinjet Edge honing machine.....	43
Fig 34) Tool Performance vs. Preparation method [19]	44
Fig 35) Regions of Solid friction	45
Fig 36) Classical friction law applies for one-direction speed.....	46
Fig 37) Comparison between uncoated and TiN coated insert [37].....	48
Fig 38) Ductile fracture stress-strain curve.....	51
Fig 39) Fracture locus for AL 2024-T351 [53].....	53
Fig 40) A schematic of Lagrangian model with tensile damage failure	55
Fig 41) ALE formulation [26].....	58
Fig 42) Number of used elements for tool and workpiece.....	60
Fig 43) sacrificial layer thickness for each edge radius	64
Fig 44) a) Thin tube turning, b) Fin cutting	66
Fig 45) Surface cleaning	67
Fig 46) Sandvik Coromant grooving tool	67

Fig 47) TPGN160302 Kennametal carbide turning insert	68
Fig 48) Schematic of plunging test	69
Fig 49) Kennametal CTCN-443-Plunging tool holder.....	70
Fig 50) Lab View user interface for force collection.....	70
Fig 51) Alicona Infinite Focus G5 Measurement System.....	71
Fig 52) Edge radius measurement- 10 μm	72
Fig 53) Edge radius measurement- 20 μm	72
Fig 54) Edge radius measurement- 40 μm	72
Fig 55) KEYENCE VHX-6000 video microscope	73
Fig 56) tool wear curve for feed= 0.05 (mm/rev)	74
Fig 57) tool wear curve for feed=100 (mm/rev)	74
Fig 58) tool wear curve for feed=200(mm/rev)	75
Fig 59) Cutting Length up to 80 μm tool wear	76
Fig 60) force spikes for feed = 0.05 (mm/rev)	77
Fig 61) force spikes for feed=0.1(mm/rev)	78
Fig 62) force spike for feed=0.2(mm/rev)	78
Fig 63) cutting force comparison for 10 μm corner radius	82
Fig 64) cutting force comparison for 20 μm corner radius	82
Fig 65) cutting force comparison for 40 μm corner radius	83
Fig 66) The temperature distribution along $f=0.05$ (mm/rev).....	85
Fig 67) The temperature distribution along $f=0.1$ (mm/rev).....	85
Fig 68) the temperature distribution along $f=0.2$ (mm/rev)	86
Fig 69) Tool reference.....	87
Fig 70) The location of maximum temperature at 10 μm cutting tool.....	88

Fig 71) The location of maximum temperature at 20 μm cutting tool..... 88

Fig 72) The location of maximum temperature at 40 μm cutting tool..... 89

Fig 73) Distance from maximum depth of crater wear 89

Fig 74) Increasing cutting feed-larger crater wear 90

List of Tables

Table 1) Johnson-Cook plastic parameters	61
Table 2) Johnson-Cook damage parameters	61
Table 3) Mechanical properties of AISI 1045 and carbide insert	62
Table 4) Thermal properties of AISI 1045 and Carbide insert	63
Table 5) Experimental work conditions.....	68
Table 6) Stress distribution on the cutting inserts.....	79
Table 7) Difference in prediction of cutting forces.....	83
Table 8) Flank wear vs. Crater wear at constant feed for different edge radius (scale bar = 300 μm).....	91
Table 9) Equivalent plastic strain contours.....	93

List of all Abbreviations and Symbols

FEM	: Finite element methods
PSDZ	: Primary shear deformation zone
SSDZ	: Secondary shear deformation zone
TSDZ	: Tertiary shear deformation zone
α	: Rake angle
γ	: Clearance angle
t_c	: Chip thickness
t	: Uncut chip thickness
φ	: Shear angle
β	: Friction angle
F_p	: Cutting force (Tangential force)
F_Q	: Feed force (Thrust force)
F_s	: Shear force
F_c	: Friction force
N_s	: Shear normal force
N_c	: Normal friction force
μ	: Coefficient of friction

K_1	: The slope of τ - σ curve in modified Merchant shear model
h_c	: Half of chip thickness
R_0	: Obstructed radius
R_n	: Natural radius
ϵ_c	: Breaking strain
BUE	: Built Up Edge
r	: Chip thickness ratio
P_m	: Machining Power
P_s	: Machining Power in PSDZ
P_f	: Machining Power in SSDZ
ρ	: Material Density
l_f	: Tool-chip contact length
Γ	: Percentage of the transmitted heat to workpiece
R	: Peclet number
C	: Specific heat

- K** : Heat conductivity
- $\frac{d\theta}{dx}$: Temperature differentiation relative to length
- θ_s : Average temperature rise in PSDZ
- θ_f : Average temperature rise in SSDZ
- θ_m : Maximum temperature rise in SSDZ
- η_m : The fraction of inelastic heat dissipation
- α : Thermal diffusivity
- β_H : Thermal Effusivity
- L_B** : Chamfer length
- γ_B : Chamfer angle
- K** : Form factor
- Δr : Shortest distance from tool tip to the ideal sharp tool
- φ : Apex angle
- $\frac{dw}{dx}$: Tool wear rate

P	: Applied load in tribometer
A_R	: Real contact area in pin and disk experiment
A_a	: Apparent contact area
B	: Wear volume
H	: Hardness
ER	: Edge radius
SL	: Sacrificial layer
CVD	: Chemical Vapor Deposition (coating)
PVD	: Physical Vapor Deposition (coating)
PFEM	: Particle finite element method
ALE	: Arbitrary Lagrangian Eulerian
VMG	: Variable microgeometry
ALE	: Arbitrary Lagrangian Eulerian
A	: a Johnson-Cook plastic model invariant parameter
B	: a Johnson-Cook plastic model invariant parameter

C	: strain rate dependency in Johnson-Cook plastic model
n	: Experimental factor in Johnson-Cook
m	: Experimental factor in Johnson-cook
$\dot{\epsilon}$: Strain rate
$\dot{\epsilon}_{ref}$: Reference strain rate in Johnson cook model
θ_{amb}	: Ambient temperature
θ_{melt}	: Melting temperature
σ_{PL}	: Plastic stress
ϵ_f	: Fracture strain
D₁	: Fracture parameter in Johnson-Cook damage model
D₂	: Fracture parameter in Johnson-Cook damage model
D₃	: Fracture parameter in Johnson-Cook damage model
D₄	: Fracture parameter in Johnson-Cook damage model
η	: Stress triaxiality
$\sigma_{Hydrostatic}$: Hydrostatic stress

$\sigma_{Von Mises}$: Von Mises stress

1. Introduction

Machining is a way to cost effectively realize dimensionally accurate parts with high surface quality. Although the role of experimental work is undeniable, the advancement of Finite Element Models has opened a new horizon to a broad range of studies to effectively evaluate parameters such as tool life and workpiece surface integrity using fundamental science. The finite element method is a numerical approach that divides the real problem into a finite number of elements and their nodes, so instead of solving a complex problem, a number of simplified elements can be solved. Once the element solutions are consolidated, the resulting model can closely approximate reality if the model is very well-defined. Although the basic ideas of Finite element method were introduced in the 1940's, its application to machining was initiated by pioneers around four decades ago. Klamecki [1] defined a 3D updated Lagrangian finite element model which could capture chip initiation. However, at the beginning of the 1980's, the application of orthogonal cutting through 2D FE models was developed by Usui and Shirakashi [2]. Iwata [3] modeled chip formation through a rigid plastic 2D model taking advantage of ductile fracture, but did not include cutting temperature in his model. Strenkowski and Carroll [4] introduced a FE model in which chip separation criteria were defined based on effective plastic strain. Lars Olovsson [5] developed the Arbitrary Lagrangian Eulerian (ALE) method for simulation of metal cutting. This method has been used by Özel et al. [6] to predict the residual stresses on finished surfaces. Arrazola et al. [7] incorporated variable friction data exported from a

pin and disk setup in the ALE model and obtained more promising results compared to using a constant friction value.

1.1 Research objectives

In this research study, the performance of various cutting tool edge radius geometries has been investigated through experimental work in order to better understand the evolution of tool wear, also corresponding FE modeling has been developed to help in selecting the cutting edge radius in an effort to maximize performance. The FE models were validated with results from experimental studies and showed good agreement. FE analysis was able to identify the cutting edge radius which would provide a high degree of performance. The updated Lagrangian model which was used in this study benefits from the use of calibrated Johnson-Cook damage parameters acquired from tensile tests. This model is particularly useful as additional calibration was not required to achieve acceptable accuracy, thus it can be used for studying various cutting conditions.

2. Literature Review

2.1 Mechanics of material removal

Metal cutting is an aggressive operation which is associated with large plastic strain, high strain rate and stresses. As Shaw [8] clearly illustrated, cutting occurs when material reaches a localized shear line in the cutting zone. This line is referred to as the shear plane. The shear plane is the plane where the material separates as a chip from a piece of material. This concept was first introduced by Merchant [9], although a deeper understanding would

be required to get agreement with experimental results. For example, they proposed that shear deformation mostly occurs along a straight line referred to as the Primary Shear Deformation Zone (PSDZ). This is a reasonable approximation under ideal conditions but since a perfectly sharp tool does not exist, and also if the material is ductile, the shear plane is not a single line but rather an area. That means that the PSDZ is an area of dislocations as shown in Fig 1.

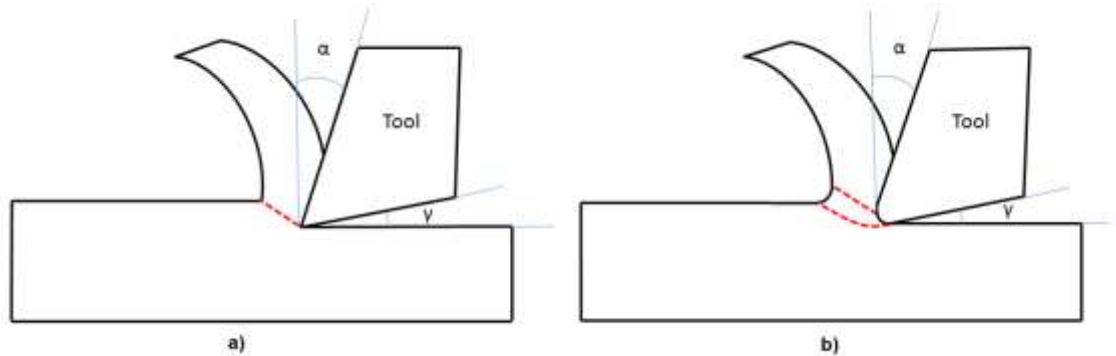


Fig 1) Shear plane for a) sharp tool, b) Rounded tool tip

It is assumed that most of the plastic deformation is in the primary region. As shown in Fig 2, the Secondary Shear Deformation Zone (SSDZ) is the interface between the tool (rake face) and chip. Sliding friction is the dominant mechanism in this area with shear deformation in this region being less than that for the PSDZ. The Tertiary Shear Deformation Zone (TSDZ), is the area where the flank face of the tool interacts with the freshly machined surface. Fig 2, clearly shows that the chip thickness is larger than the uncut chip thickness ($t_c > t$). The explanation of this phenomenon lies in how the material effectively stacks up after the PSDZ forcing the chip to be greater in thickness than the

uncut material entering the cutting area. Based on the material volume conservation law the chip length then is also shorter than the uncut chip length. This is required in order to keep the material volume constant.

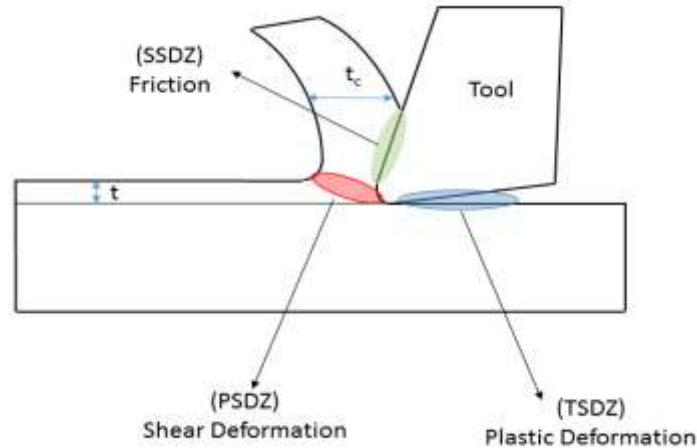


Fig 2) Deformation zones in metal cutting

2.2 Oblique cutting vs. orthogonal Cutting

In any of cutting operation in which the cutting edge and cutting motion are not in the same direction and make an angle with each other, oblique cutting is established. This also occurs if chip flow (V_c) and cutting motion are in different directions. Thus, simulation of this kind of cutting requires the use of 3D models. For the sake of simplicity, orthogonal cutting has been used in either numerical or analytical simulations. Examples of this kind of operation are broaching, sawing and planing. In orthogonal cutting, it is assumed that there is no material flow in the third dimension and all deformation during cutting happens in two dimensions. Consequently, modeling of cutting operations in this configuration is easier to perform.

The following assumptions are the prerequisites of orthogonal cutting operations [8]:

1. A perfectly sharp tool which does not have any contact with the machined surface,
It should be noted this assumption is the foundation of the analytical models such as Merchant and Lee & Shaffer, otherwise Primary Shear Deformation Zone (PSDZ) will not be a straight line, as mentioned in “Theory of Deck of Cards”, by Piispanen (1937),
2. The tool cutting edge is perpendicular to the cutting motion, as mentioned above,
3. No material deformation in the third dimension means material strain will be zero as well, which then corresponds to 2D plane strain,
4. The width of the cutting tool should be larger than the workpiece width so that it overhangs on both sides as shown in Fig 3.

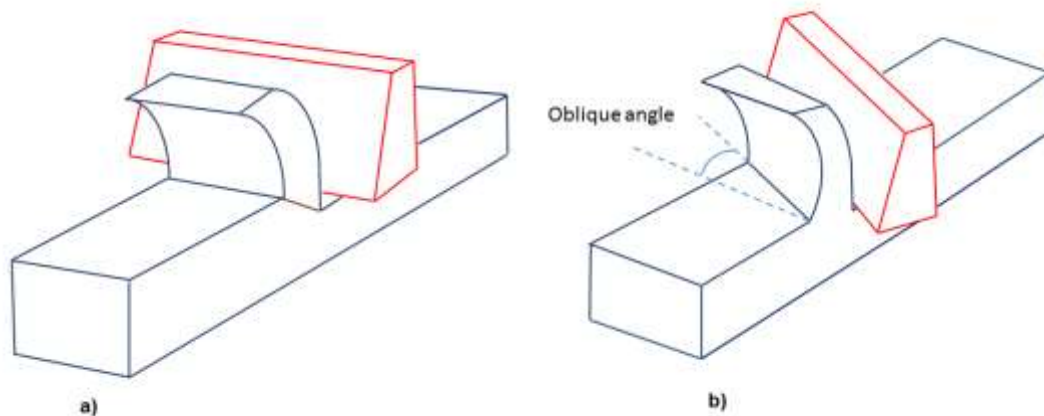


Fig 3) a) Orthogonal Cutting b) Oblique cutting

2.3 Analytical Models:

2.3.1 Merchant Model

Assuming that shearing occurs through a straight line, Merchant (1945) considered that the chip layer is in equilibrium when the resultant force (\mathbf{R}) at the tool-chip interface in the SSDZ and resultant force at the PSDZ (\mathbf{R}'). Thus $R=R'$.

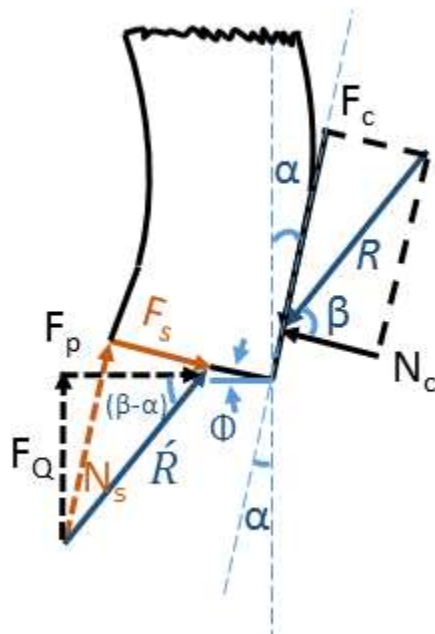


Fig 4) Chip free diagram

In Fig 4, ϕ , β and α are the shear angle, friction angle and rake angle respectively, F_c and N_c are friction force and its normal, F_s , N_s are the shear and normal forces and F_p , F_q are the cutting force and thrust force as measured by a cutting force dynamometer. Interestingly, Merchant organized the forces such that there is a circle of diameter R which covers the shear, cutting and frictional forces. This circle is known as the Merchant Circle,

and is shown in Fig 5. Analytical relationships between forces can be derived using this circle.

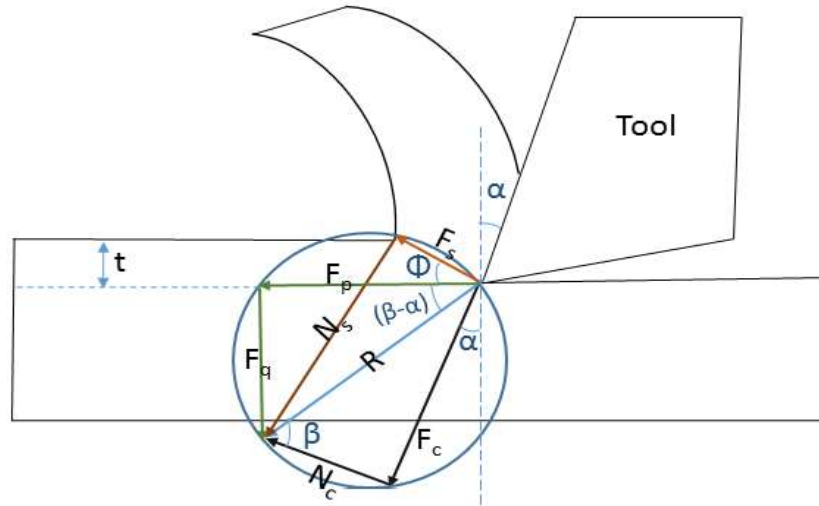


Fig 5) Merchant Circle

By looking at Fig 5, F_p and F_q can be extracted based on F_s :

$$F_p = \frac{F_s \cos(\beta - \alpha)}{\cos(\phi + \beta - \alpha)} \quad (1)$$

$$F_q = \frac{F_s \sin(\beta - \alpha)}{\cos(\phi + \beta - \alpha)} \quad (2)$$

Also from the chip diagram, the shear plane area can be obtained by the following equation:

$$A_s = b t / \sin\phi \quad (3)$$

By plugging Eq (3) in to Eq (1) the following equations for F_p and F_q can be found:

$$F_p = \frac{\tau b t \cos(\beta - \alpha)}{\sin\phi \cos(\phi + \beta - \alpha)} \quad (4)$$

$$F_Q = \frac{\tau b t \sin(\beta - \alpha)}{\sin\varphi \cos(\varphi + \beta - \alpha)} \quad (5)$$

Within F_p cutting force, F_Q feed force, t is the uncut chip thickness, τ is the shear strength of the workpiece material, b is the width of the cut. φ , β and α are shear angle, friction angle and rake angle respectively. After full analysis, the following equations can be extracted:

$$F_s = F_p \cos\varphi - F_Q \sin\varphi \quad (6)$$

$$N_s = F_Q \cos\varphi + F_p \sin\varphi \quad (7)$$

$$F_c = F_Q \cos\alpha + F_p \sin\alpha \quad (8)$$

$$N_c = F_p \cos\alpha - F_Q \sin\alpha \quad (9)$$

Accordingly the Coulomb coefficient of friction can be calculated as shown below:

$$\mu = \frac{F_c}{N_c} = \frac{F_Q \cos\alpha + F_p \sin\alpha}{F_p \cos\alpha - F_Q \sin\alpha} = \tan\beta \quad (10)$$

Shear angle is a determinative cutting parameter in that other parameters dependent on it. The larger the shear angle, the smaller the chip thickness, which then requires less cutting energy to form and break it off of the workpiece. Merchant relied on the minimum energy law and assumed that cutting energy should be minimum. So if cutting speed and shear strength are constant then:

$$\frac{d(F_p V)}{d\varphi} = \frac{d}{d\varphi} \left(\frac{V \tau b t \cos(\beta - \alpha)}{\sin\varphi \cos(\varphi + \beta - \alpha)} \right) = 0 \quad (11)$$

$$\frac{d}{d\varphi} ((\sin\varphi \cos(\varphi + \beta - \alpha)) = 0 \quad (12)$$

By using the knowledge of trigonometric relationships, after derivation, the equation will be displayed as follows:

$$\cos(2\varphi + \beta - \alpha) = 0 \quad (13)$$

$$2\varphi + \beta - \alpha = \frac{\pi}{2} \quad (14)$$

Eq (14) is the solution that Merchant offered to predict the shear angle. The weakness of this model is that material properties have not been considered. In the modified version of the Merchant model, the shear strength of the material is not constant but is dependent on normal stress.

$$\tau = \tau_0 + k_1\sigma \quad (15)$$

Based on this assumption and performing the same procedure as above, the shear plane solution will be derived as shown below:

$$2\varphi + \beta - \alpha = \cot^{-1} k_1 \quad (16)$$

2.3.2 Lee and Shaffer

In this model it is assumed in PSDZ orthogonal lines which are called slip lines corresponding to maximum shear stress which is intuitive from Mohr's circle diagram. Also, slip lines meet the free surfaces at 90° which corresponds to 45° in the 2D plane surface. A free surface is a surface where both the normal and shear normal surface are equal to zero, so it will be the coordinate origin. By looking at Mohr's circle solution, the following relationship can be obtained:

$$\varphi + \beta - \alpha = 45 \quad (17)$$

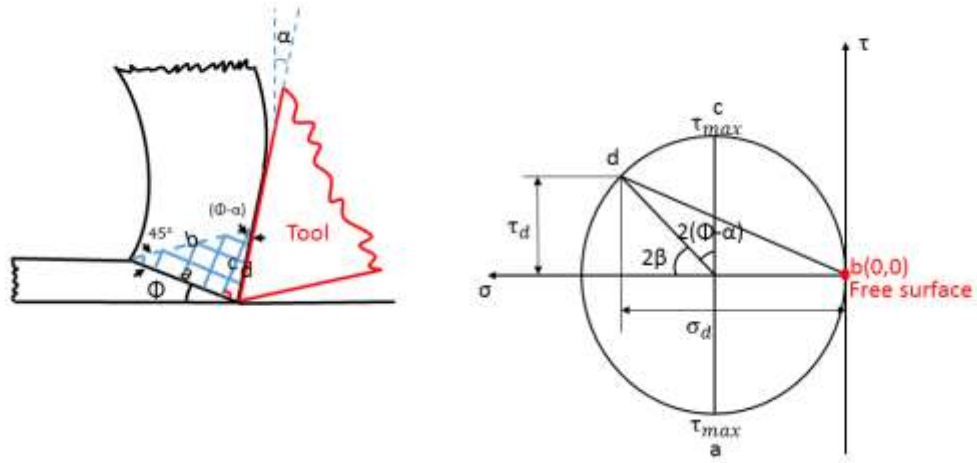


Fig 6) Lee and Shaffer shear model based on Mohr's circle

This also can be verified by the assumption that F_s is in the direction of maximum shear stress and R is in the direction of principal stress Fig 7 as mentioned above that the angle between principal stress and maximum shear stress is 45° . With this the same expression shown in Eq (17) will be obtained.

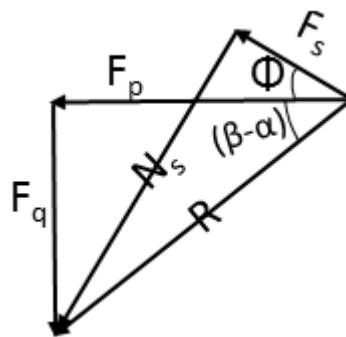


Fig 7) Proof of Lee and Shaffer

Although this model is still used as an analytical solution, it is not able to predict reasonable values for the shear angle at a zero rake angle and for a friction angle equal to 45° as we have:

$$\varphi = 0 \quad (18)$$

Which is not an acceptable value for shear angle.

2.4 Chip formation

A chip is a hardened and brittle flake of material which is curled due to shear failure in PSDZ which was outlined in detail in the previous section. Knowledge of chip morphology is vital for machinists, researchers, and scientists as it helps them understand what is happening in the cutting zone. Chip formation is dependent on cutting conditions such as cutting speed, feed, and depth of cut, material being cut and cutting insert geometry. Lack of knowledge in this area could cause low productivity due to rapid tool failure, and poor surface finish because of thermal errors and dimensional inaccuracies. Further, as the chip is harder and sharper than the workpiece material after it undergoes large plastic deformations, conditions such as chip jamming can cause scratches on the workpieces and thus increase the surface roughness.

Chips are formed in different shapes depending on cutting conditions. There are four descriptors generally used, which are:

- 1- Continuous
- 2- Discontinuous (segmented)
- 3- Continuous with Built up Edge (BUE)
- 4- Saw tooth chips.

Continuous chip formation is common in the cutting of ductile materials such as mild steels (AISI 1045) and aluminum, especially at high cutting speed when the material softens under the high temperatures associated with high speed cutting. Segmented chips are formed in brittle materials (cast iron) and materials with low thermal conductivity like (Titanium) at a low cutting speed and a high cutting feed. In continuous chips with BUE, normally high friction and low cutting speeds lead to adhesion of fragments of the workpiece material to the cutting tool. BUE, however, is an unstable piece of material which breaks off and forms cyclically over time. Saw tooth chips are semi-continuous chips with high and low shear deformation areas which normally result in the formation of discontinuous chips. However, because of the high normal stresses in the PSDZ, the cracks which form are closed and semi continuous chips are formed. This type of chip, which is also known as a lamellar chip is formed mostly in hard-to-cut materials, such as hardened steels, which are machined under a high cutting speed. Also, when the rake angle is negative, the chance of this kind of chip forming is high.

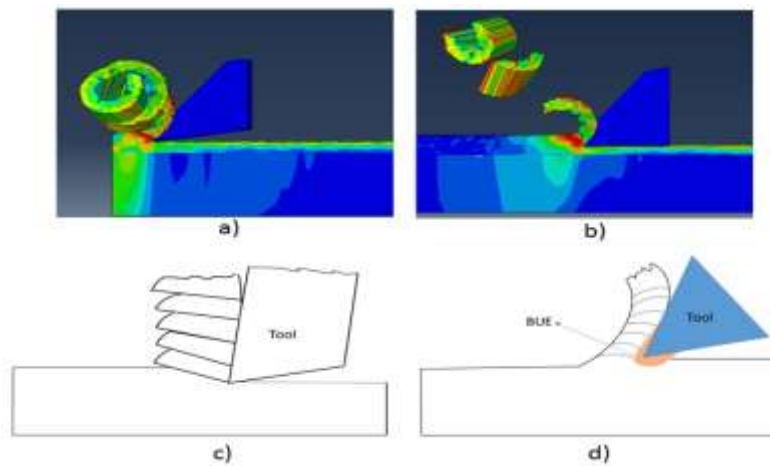


Fig 8) chip types, a) continuous chip b) Discontinuous chip c) Saw-tooth chip d) Continuous with BUE

Although the chip itself is not significantly important in a machining operation as it is generally recycled, the management of it still represents a cost factor in production and its formation is one of the best signs of whether the cutting conditions are appropriate or not. For example, as can be seen in Fig 9, the spectrum of blue colours on the chip resulting from cutting AISI 1045 in the plunging test, which was done in this study relate to temperature. It is important to know that, by increasing cutting speed, heat will be dispersed more into the chips than the tool or workpiece so, as can be seen in Fig 9 at a high cutting speed of 400 and 500 m/min chips, a high temperature results as shown by the spectrum of blue colours. The use of chip colour to assess machining temperature was mentioned by Nakayama [10]. This phenomenon, which is called bluing results when heat builds up in the chip and for this material increases the fracture toughness of the chips so they are more ductile and thus harder to break. Normally, higher chip stiffness (brittleness) helps to break the chip easily.



Fig 9) Hard to break chips generated from AISI 1045

K. Nakayama [10] claimed that the chip breaks when the bending strain reaches a specific value called ϵ_c and the following relationship was proposed by him:

$$h_c \left(\frac{1}{R_0} - \frac{1}{R_b} \right) \geq \epsilon_c \quad (19)$$

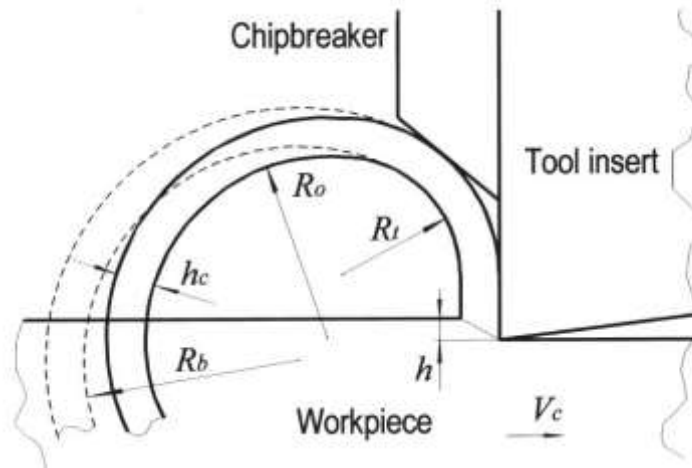


Fig 10) chip formation by using chip breaker [11]

Where h_c is half the chip thickness, R_0 is the natural chip radius, which is the natural curl form of the chip without using any chip breaker, while, R_b is the radius of chip curl after using a chip breaker or applying a bending moment. From Eq (19), one can conclude that chip breakage can be facilitated by increasing h_c or chip thickness, and that can be done by increasing uncut chip thickness (feed in our study). Another way is to reduce the breaking strain (ϵ_c), which can be done through the use of cryogenic coolant in machining, alloying, or other processes that increase the brittleness of the chip and facilitate chip breakage. Last but not least, using a chip breaker can help to reduce R_b . It is important to mention that if:

$$R_b = R_0 \quad (20)$$

The left side of the non-equation will be zero, which means the chip will never break. Fig 11 Fig 10, illustrates an example of this situation in this study where the length of chip reaches 150 cm when carbide inserts that do not have a chip breaker were used.

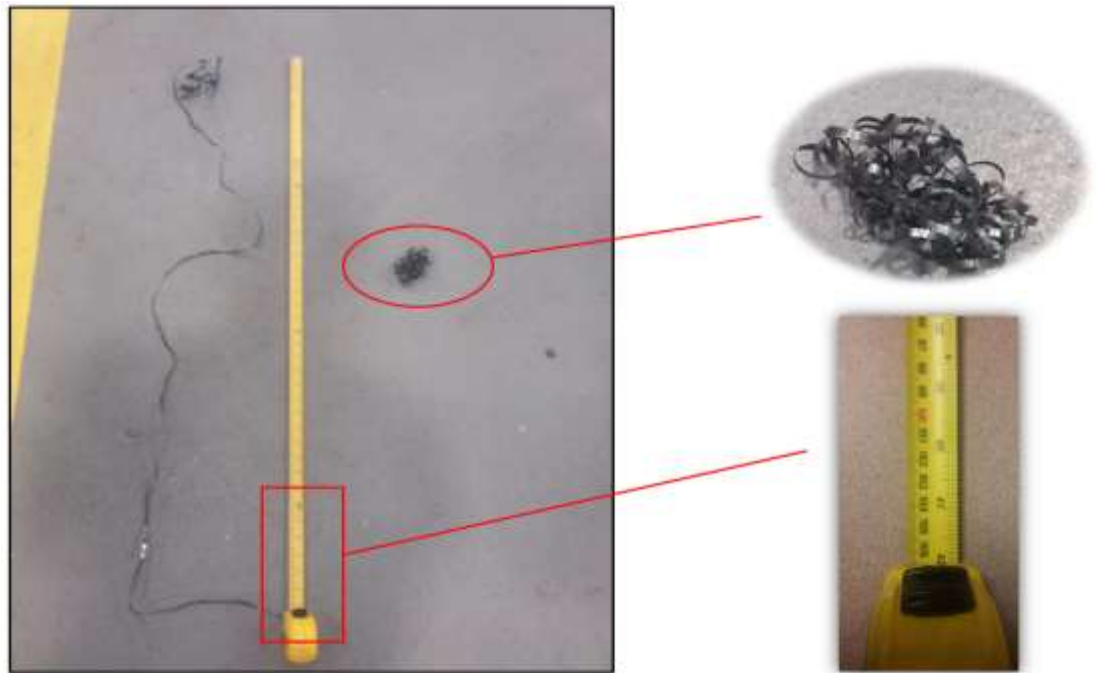


Fig 11) non-breakable chips in the left side vs. chip jamming in the right side in same operation

Traditionally, to study chip formation, researchers have used a quick-stop device as shown in Fig 12, which was first used by Boothroyd [12]. This mechanism is designed so that it can withstand cutting forces but once the tongue engages the pins embedded inside the mechanism are sheared and freeze the chip in the cutting zone, which is already formed along the tool rake face, is preserved. Capturing cutting forces through experiments and looking for sudden changes or any discontinuity or fluctuation in the force can be used to identify where chip breakage is occurring. For example, Zhang et al. [13] determined that

an increase in cutting speed increases the chance that saw-tooth chips are forming in Inconel 718, and this is the main reason for force fluctuation in this process. However, one of the most efficient ways to study chip morphology is with the finite element method. Ashwin Devota et al. [14] studied the effect of rake angle and feed on chip formation of AISI 1045 using the finite element method. This research showed the importance of stress triaxiality in predicting chip formation accurately.

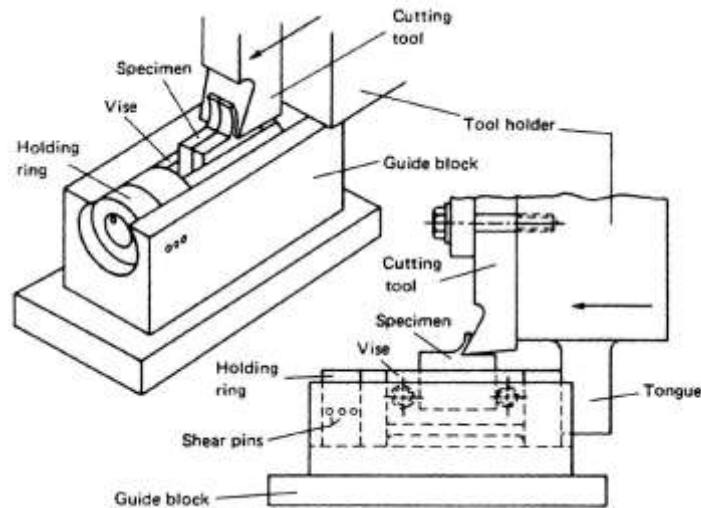


Fig 12) Quick stop device [12]

2.5 Temperature in machining

Temperature rise is the outcome of plastic deformation, and in some studies, it is considered that almost one hundred percent of plastic work is converted to heat in the process. Temperature has a dominant effect on tool life and, similarly, on the workpiece surface integrity compared to other factors. Studies showed that the largest portion of cutting energy is consumed in the PSDZ (75%) which means that most of the heat is being

generated in this region. Depending on the heat transfer values for the material this heat energy is conducting back into the workpiece or the tool or remains with the chip. The rest of the cutting energy (25%) is being consumed to overcome friction in the SSDZ. As the tool wears out, the contact area between the tool flank face and the freshly machined surface increases, as the area associated with the TSDZ grows it contributes more to heat generation and also heat transfer into the tool and workpiece. Increasing the machining speed has been shown to increase the cutting temperature [15]. Accordingly, for materials such as low carbon steels, Aluminum, etc., cutting speed can be very high approaching 1000m/min, while for materials like Titanium cutting speeds are generally in the 50m/min range. Titanium alloys are poor conductors of heat thus most of the heat generated in these applications will be conducted into the cutting tool, resulting in temperature build up in the tool leading to faster tool wear. Thus, cutting speed is a limiting factor for these kinds of materials. The question here is that, if most of the energy exchange in the PSDZ is almost three times that in the SSDZ, why is the location of the maximum temperature on the rake face? To explain this phenomenon, Boothroyd [12] in Fig 13 illustrates that if one point, such as Y, crosses the PSDZ and moves along the rake face, it is in contact with the rake face for an extended period of time. Accordingly, the area of heat conduction with the tool is much larger than the PSDZ, so the maximum temperature is located on the rake face. The distance of this point from the tool tip depends on the contact area of the tool with both the chip and the machined surface. The closer the maximum temperature is to the tool tip, the more unfavorable it is because the cutting edge will be more prone to tool wear, and this heat disperses more to the workpiece than to the chip as mentioned earlier. Astakhov

[16] claimed that, by increasing cutting speed and maintaining relative tool sharpness, more of the heat generated can be dispersed to the chip (80-90%), with 5-10% going to the workpiece and the remaining 5-10% going to the tool. That is why increasing the cutting speed does not necessarily increase the temperature at the tool chip interface as more heat is going out with the chip.

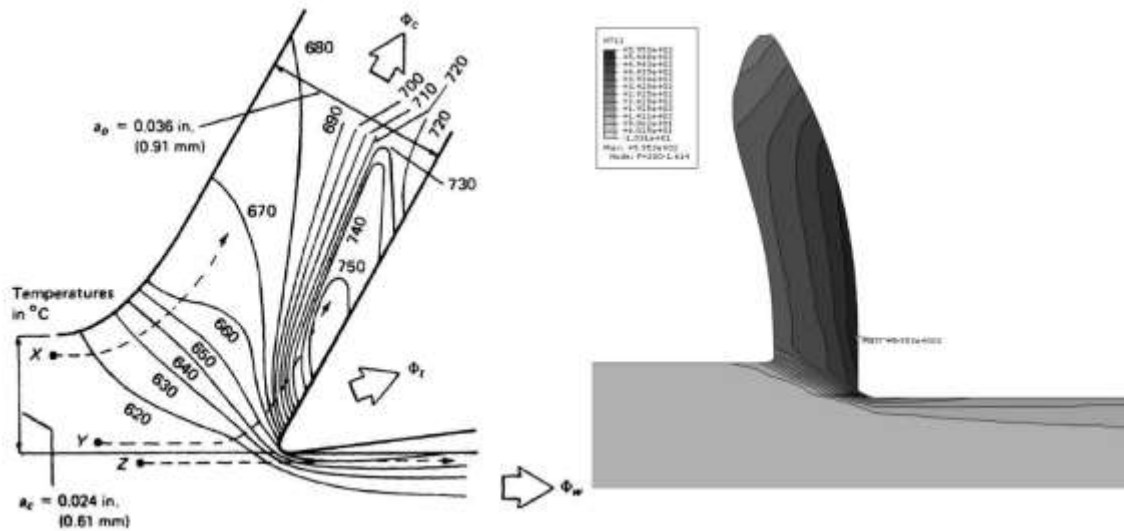


Fig 13) Temperature profile captured by infrared camera [12] vs. FEA

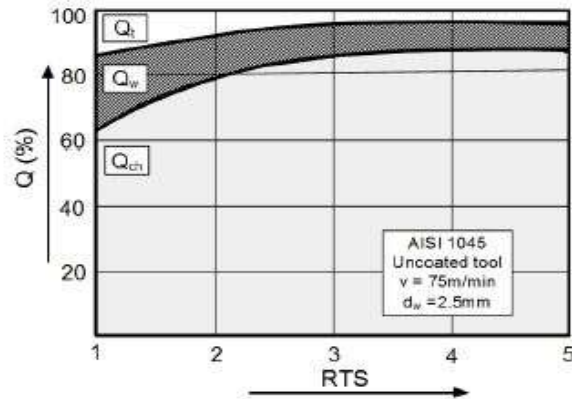


Fig 14) Heat dissipation percentage to tool, workpiece and chip [8]

As mentioned earlier, in metal cutting, heat transfer is the energy derived from plastic deformation. Abukhshim et al. [17] simply considered that the plastic energy will be fully converted to heat so:

$$P_m = F_p \cdot V \quad (21)$$

$$P_f = \frac{F_c \cdot V}{r} \quad (22)$$

Where P_m is the heat converted in the PSDZ, F_p is the tangential force, V is the cutting speed, P_f is the converted heat in the SSDZ, which should be calculated based on the frictional force (F_c), and r is the chip thickness ratio.

$$P_m = P_s + P_f \quad (23)$$

Boothroyd [12] assumed that the percentage of the heat is transmitted to workpiece (Γ) and $(1 - \Gamma)$ of that is dispersed to the chip. Where Γ is obtained from the following empirical equation:

$$\Gamma = 0.15 \ln \left[\frac{27.5}{R \cdot \tan \varphi} \right] \quad (24)$$

Where φ is the shear angle and R is a non-dimensional parameter called the Peclet number [18]:

$$R = \frac{V \cdot t \cdot b}{k / \rho \cdot c} \quad (25)$$

In this relation, V , t and b are cutting velocity, the uncut chip thickness and the workpiece width respectively, K is heat conductivity, and ρ and c are density and the specific heat of

the material used. This dimensionless parameter interestingly displays the predominant mechanism of heat transfer, which could be either due to physical transportation or conduction. Boothroyd [12] assumed that heat transfer inside a material happens through these two methods. Transportation occurs when the hot material flows so it has speed, while in conduction, velocity is not required but is rather controlled by the material's thermal conductivity. So Q_1 and Q_2 are heat transfers through conduction and transportation respectively:

$$Q_1 = -kA \frac{d\theta}{dx} \quad (26)$$

$$Q_2 = \rho cvA \bar{\theta} \quad (27)$$

Where $d\theta/dx$ is the differentiation of temperature over a known distance, $\bar{\theta}$ is the average temperature and A is the area of heat transfer. Thus, it is now clear that the Peclet number incorporates the transportation heat transfer mechanism in its numerator and heat conduction is placed in the denominator. So, by increasing speed, this parameter will increase, which shows that transportation is dominant at a high cutting speed as there is insufficient time for conduction inside the material.

He then obtained the following equations for temperature rise at the PSDZ, SSDZ and within the chip itself:

$$\theta_s = \frac{(1 - \Gamma) \cdot P_s}{\rho cvtb} \quad (28)$$

$$\theta_f = \frac{P_f}{\rho cvtb} \quad (29)$$

$$\theta_m = 1.13 \theta_f \sqrt{\frac{R \cdot t_c}{l_f}} \quad (30)$$

θ_s , θ_f and θ_m are the average temperature rise in PSDZ, SSDZ and maximum temperature rise in the SSDZ. L_f is tool chip contact length, which can be obtained from the following equation:

$$\frac{l_f}{t_c} = 1 + \tan(\varphi - \alpha) \quad (31)$$

Finally the maximum temperature on the chip is achieved by the aggregation of all mentioned temperatures plus θ_0 , which is the ambient temperature.

$$\theta_{max} = \theta_m + \theta_s + \theta_0 \quad (32)$$

The parameter called thermal diffusivity is a specific feature of each material which exhibits its response to the temperature difference. In simulation, as machining is a high speed process instinctively heat transfer between elements and surrounding area can be neglected. Hence, this process is assumed to be adiabatic and heat transfer will be occurred just between the tool and the workpiece.

$$\alpha = \frac{k}{\rho C_p} \quad (33)$$

In this equation, k is the thermal conductivity, ρ is the material density and C_p is the specific heat capacity. In contrast, the parameter thermal effusivity (β_H) is the capacity of each material to absorb the heat and can be defined as the ratio of heat absorption of the

workpiece to the one of the tool. In other words, this parameter reflects what share of the heat leads to the temperature rise of the tool (master) and that of the workpiece (slave).

$$\beta_H = \frac{\sqrt{\rho_s C_s K_s}}{\sqrt{\rho_s C_s K_s} + \sqrt{\rho_m C_m K_m}} \quad (34)$$

By plugging the average values from Table 3 and Table 4 for both tool and workpiece in this equation β_H can be obtained from Eq (35). This value is being used as the input in the simulation.

$$\beta_H = \frac{13961}{11036.3 + 13961} = 0.558 \sim 0.56 \quad (35)$$

It has been assumed in many studies, such as [12], [13] that 90% of the energy consumed for inelastic dislocations is converted to heat, so by saying that, in Eq (35), the fraction of inelastic dissipation rate (η_m) was set to 0.9

$$Q_{pl} = \eta_m \sigma \dot{\epsilon} \quad (36)$$

Where Q_{pl} is the transferred heat because of plastic deformation, σ is the plastic stress and $\dot{\epsilon}$ is the plastic strain rate.

2.6 Cutting Edge Geometry

The tool geometry in the machining process is a significant parameter which affects not only the tool longevity, required cutting forces and temperature but it plays a very important role in surface quality, residual stress and surface integrity in general. As the tool moves

through the workpiece it cuts the material along at least two surfaces. So except for specific applications such as with orthogonal cutting, each cutting tool should have at least two cutting edges to ensure proper chip formation. These cutting edges are: 1- Main cutting edge 2- Auxiliary cutting edge. In one geometry categorization, the cutting inserts are divided into single-point cutting inserts such as turning, boring, planning, etc. and multiple point cutting edges such as milling, drilling, tapping and reaming, which is not part of the scope of this study. A single point cutting insert can come in three different clamping shapes: 1-solid single point cutting tool, which is not very common in advanced machining but was used on manual lathes. 2- Cutting inserts with brazed inserts, which involves cutting insert material brazed onto the tool shank. 3- Cutting inserts which are clamped to the tool shank, Fig 15.

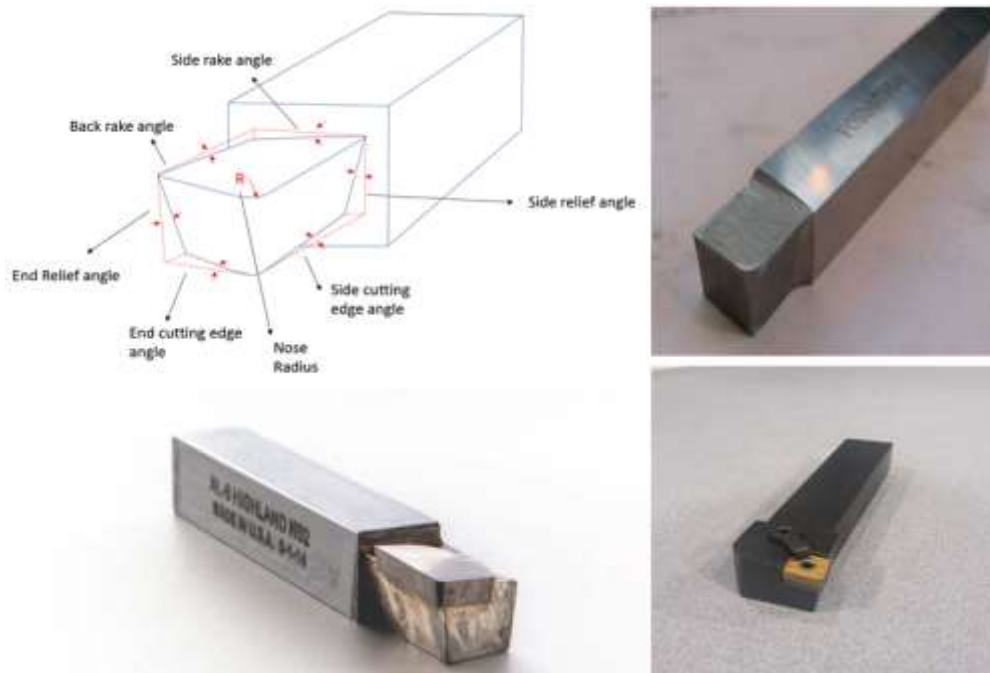


Fig 15) Different types of single point turning inserts

In another categorization, cutting tools are generally divided into three groups: 1-Sharp edge tool, 2-T-Land/Chamfer edge and 3-Hone/round edge [14]. Cutting tool edge definition is a comprehensive observation of the cutting tool performed with both macroscopic and microscopic characteristics [15]. Macroscopic geometry features are the ones by which each cutting tool is known commercially, such as rake angle and nose radius. Rake angle is the angle that the rake face makes with the vertical line and the clearance angle is the angle between the flank face and horizon line, Fig 16. Negative rake angle inserts are prevalent where the workpiece material is hard-to-cut, such as hard steel, as the cutting insert is required to be strong enough to withstand high cutting forces, while positive rake angle inserts are mostly designed for softer materials such as Aluminum, which can facilitate chip formation.

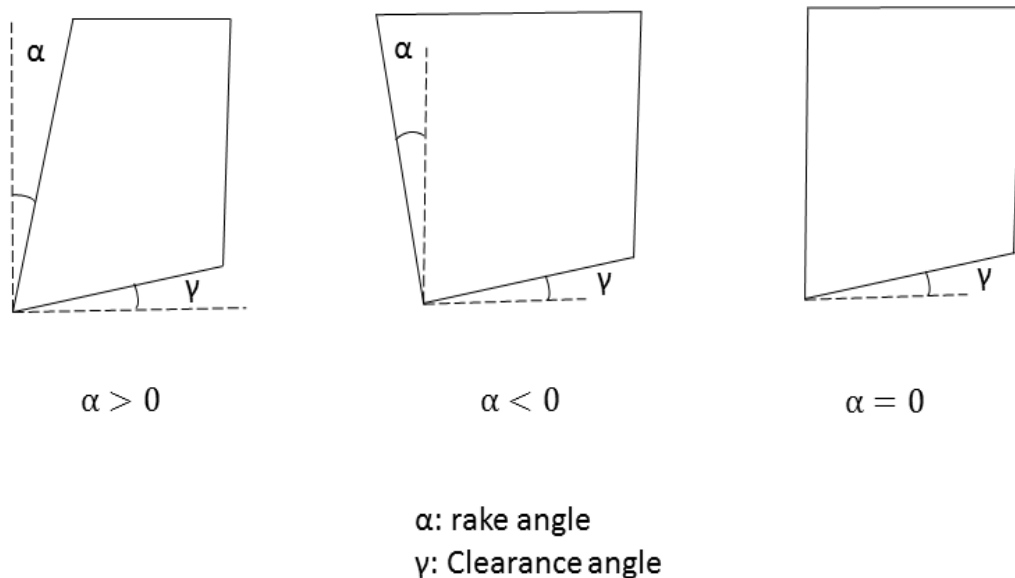


Fig 16) Definition of tool angles

Microscopic features are actively involved in the cutting operation and minor changes in these parameters lead to a significant difference in terms of cutting performance. This example, proposed by Denkena and Biermann [19] in Fig 17 can clarify the difference between these parameters. As can be seen, the rake angle is positive on the macroscopic scale while right at the cutting edge in the small scale, a large portion of the cutting tool in the transition area between the rake face and the flank face exhibits an effectively negative rake angle. So it should be considered that an ideal sharp tool does not exist, and tool bluntness can directly affect cutting forces, surface integrity, etc. Denkena and Biermann [19] also mentioned that, for a decade, a broad area of research has been dedicated to cutting tool microgeometry characterization.

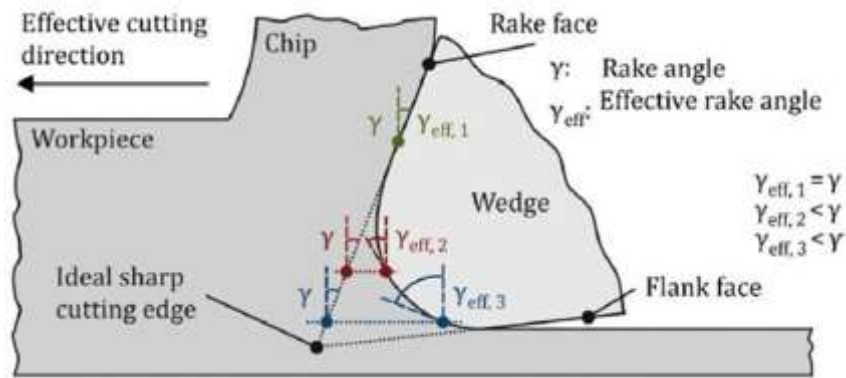


Fig 17) Macroscopic and Microscopic features of a cutting insert [19]

A chamfer is a microgeometry feature which can be defined by a chamfer length l_β and chamfer angle γ_β . See Fig 18 for details. While edge radius measurement still is a big challenge as it is difficult to define with a unique value.

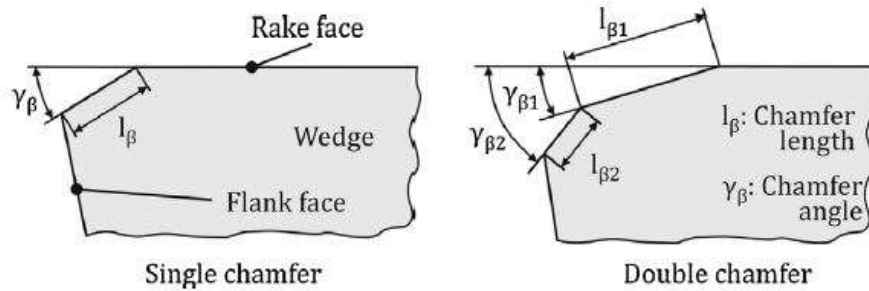


Fig 18) Chamfer geometry characterization [19]

Traditionally, in order to measure the cutting edge radius a circle where the intersection of flank and rake face could be approximated by at least three data points and edge radius could be measured. However, for asymmetrical shapes due to wear, chipping, burr and coating imperfection, one unique value for edge radius cannot be applied. As seen in Fig 19. Increasing the number of data points on the cutting edge radius increases the accuracy, but the method of fitting and the number of measured data points depends on the user, which can change and is thus not consistent.

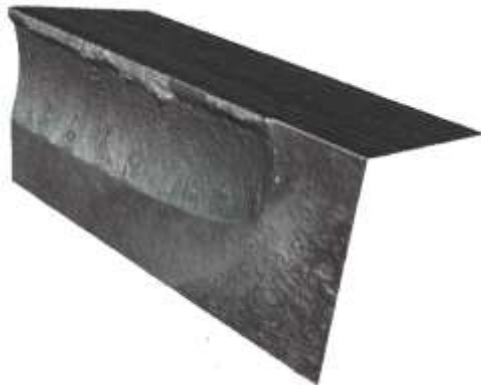


Fig 19) Worn tool surface irregularities

Denkena and Biermann [19] proposed a more reliable method to measure edge radius which was referred to as a Form Factor (K-factor), which assigns three values instead one value to measure edge radius.

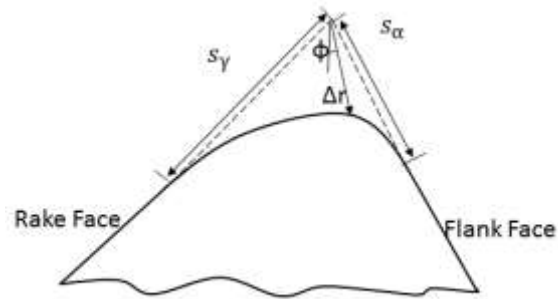


Fig 20) K- factor method for cutting edge characterization [19]

In Fig 20 s_α and s_γ are the cutting edge segments on the flank face and rake face, respectively, Δr is the shortest distance between the actual tool to the ideal sharp tool, and its corresponding angle ϕ (Apex angle) are both indications of the bluntness of the cutting tool compared to an ideal sharp tool.

$$\bar{s} = \frac{s_\alpha + s_\gamma}{2} \quad (37)$$

$$k = \frac{s_\gamma}{s_\alpha} \quad (38)$$

Here \bar{s} is the average cutting edge radius and k is called the Form Factor which shows the orientation of the radius to either a flank or rake face. This method facilitates tool edge radius measurements, in particular for asymmetric geometries. However, there is still uncertainty in finding flank and rake face tangents. Rodriguez [20] also introduced a

method based on fitting a polynomial of sixth degree on the cutting edge, however, the main disadvantage of this method is the high deviation between the fitted polynomial and the actual edge radius. Another idea, proposed by Uhlmann et al. [21] was a detailed tool geometry characterization which considers tool edge geometry and uncut chip thickness simultaneously. This method has been followed by other researchers by looking at tool engagement at the micro scale compared to tool edge radius $\left(\frac{h_{tr}}{r_\beta}\right)$ Fig 21. This method is a comprehensive approach to finding the active microgeometries which are involved in cutting, however, again, its dependency on edge radius (r_β) and inaccuracy in measurement still exist.

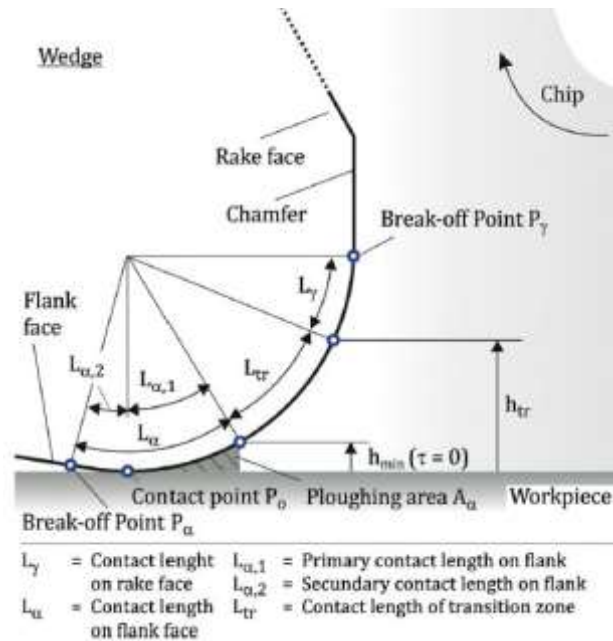


Fig 21) Uhlmann method for edge radius characterization [19]

Looking at recent literature, it is evident that Denkena and Biermann's idea is still prevalent among researchers, so the appropriate data has been extracted for this method from the

Alicona Infinite Focus microscope, used for the edge radius measurements in this study. The setup associated with this measurement is built into the software provided by Alicona. This will be detailed in the Experimental work chapter

2.6.1 Chamfered Tools

The purpose of using a chamfer on the cutting edge is in having two or more effective rake angles engaged in the cutting zone. Normally the first one or two rake angles are negative and can reinforce the tip of the tool against concentrated forces compared to a sharp one, while the main rake face is still positive [22]. By doing this premature tool breakage can be avoided and there is a better heat transfer rate compared to a bulky tool with a negative rake face. However, a small chamfer with a negative rake face also can create a region beneath itself which is called a “Dead Metal Zone (DMZ)”, which not only increases the cutting forces, but also affects the dimensional accuracy of the final part due to the variation of DMZ size during the machining process as reported by [22], [23].

Yen et al. [24] developed a FE model and applied in a comprehensive study on tool edge effects studying parameters such as cutting forces, temperature profile, shear and normal stress distribution at the tool-work interface. The results clearly showed that by increasing both the chamfer angle and width, cutting forces will be increased with more effect on thrust forces due to the larger projected length on the flank face.

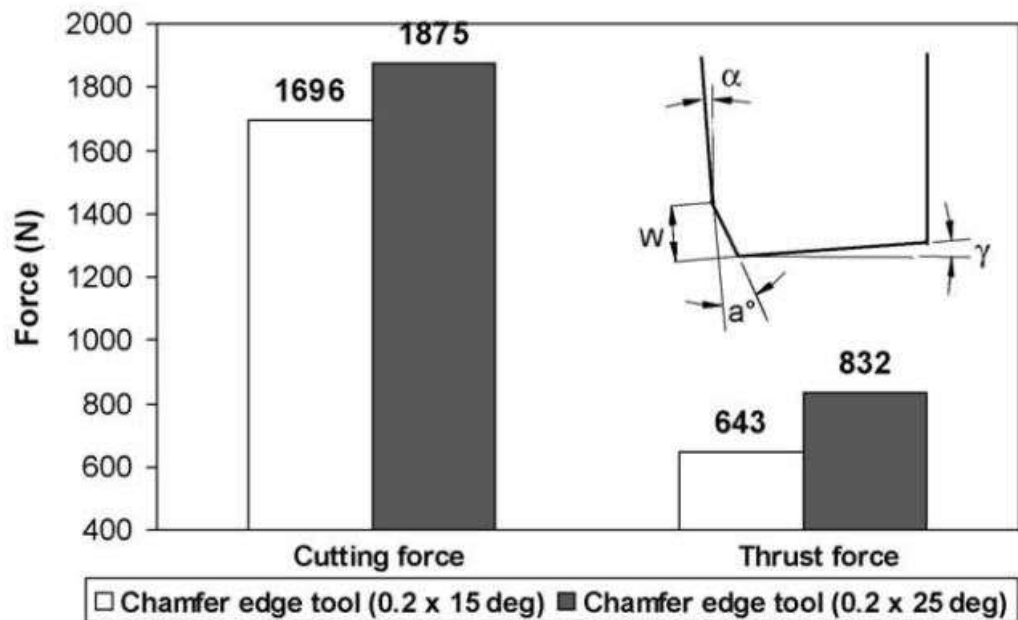


Fig 22) The effect of chamfer angle on cutting forces [24]

They showed that the temperature profile is also sensitive to the chamfer edge angle and width, with the maximum temperature occurring at the upper chamfer corner. However, as this value becomes larger, the maximum temperature will be shifted to the lower chamfer edge where the tool tip is located. Thus, by increasing the chamfer edge and angle, the maximum temperature will be larger and the temperature profile will be moved to the flank face.

2.6.2 Honed tools

In this study, the effect of a variation in the tool edge radius on the cutting forces, temperature and stresses have been studied. Increasing the edge radius has a significant effect on the cutting forces, mostly on the thrust forces, as the effective rake angle is

negative and the ratio of (t/t_c) becomes larger, which results in a plowing effect and respectively more cutting energy and forces will be consumed to remove the material. The plowing effect has an adverse impact on the surface, as the surface roughness increases. Since a larger edge radius can cause greater plastic deformation or a greater friction area [25], this, in turn causes more generated heat which will be transferred to the work and tool, and then higher temperature will be attained. On the other hand, a larger edge radius provides wider area for heat conduction which results in a lower temperature. Hence, these results created an opportunity for the optimization of the edge design. Cutting edge radius variation can also affect the surface integrity, for which residual stress is a determinative parameter. Based on the literature, the machining of AISI 316L was studied both numerically and experimentally by [25]. As mentioned above, larger edge radius leads to greater plastic deformation and a higher temperature which plays an important role in increasing the tensile residual stress on the workpiece surface, followed by more compressive stress in deeper layers of the workpiece material. By plotting a velocity profile, Nasr [25] noticed that the stagnation zone is a triangular shaped area close to the tool tip which, by increasing edge radius, will be extended. Interestingly, the stagnation zone tip, called the stagnation point, for all the edge radii was the same distance (T) from rake face, while its distance from the machined surface (h) became larger Fig 23. The same trend for the residual stress was observed by others [26] for high speed machining of AISI 4340 and for cutting forces and temperature for the coated carbide tools as observed by Al-Zkeri et al. [27]. Although the direct relationship between cutting forces and edge radius were verified by all the mentioned research studies, this was not the case all the time as reported

by Fulemova and Janda [28]. In their project, they measured tool wear and cutting forces for three different edge radius geometries: 5, 10 and 15 μm . As it was expected, the sharper the edge was, the more wear they observed. The same trend was seen for surface roughness, with the exception of 10 μm as it had more defects on the tool edge compared to the sharp one. Interestingly, force measurement results showed that for reducing edge radius 15, 10 and 5 μm cutting forces increases respectively, and this is due to the higher wear rate of the sharper tool as compared to others.

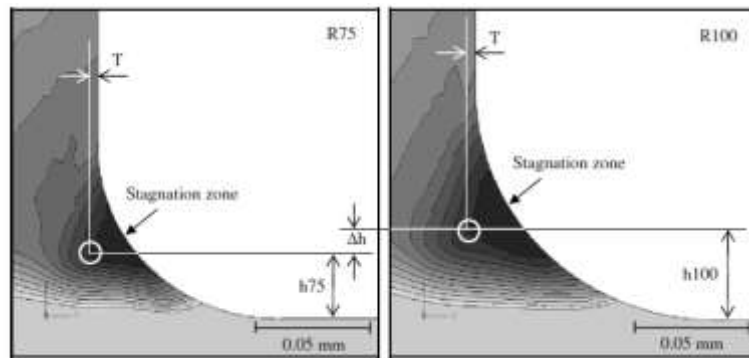


Fig 23) Stagnation point distance for a) R75 b) R100 [25]

Subbiah and Melkote [29] studied the effect of edge geometry on material deformation in the cutting zone. In their study they used a “quick stop device” similar to the one introduced earlier in this thesis. This setup stops the machining operation and freezes the chip while it is still attached to the workpiece. Thereafter, the cutting zone is removed by wire EDM and mounted in an epoxy polymer. All the collected samples were polished, and this process was completed by etching. He observed that the tool tip engages with the workpiece as the material is mostly under tension and three situations may occur: 1- The workpiece material is ahead of the upper and lower part of tool edge radius and both sides are in equal tensile

force, so fracture happens in the middle, 2-Tensile force is stronger in the upper side (or material is weaker), so fracture will happen at the upper side of the mentioned region, and 3-Tensile force is stronger at the lower side, and fracture will occur on the lower side.

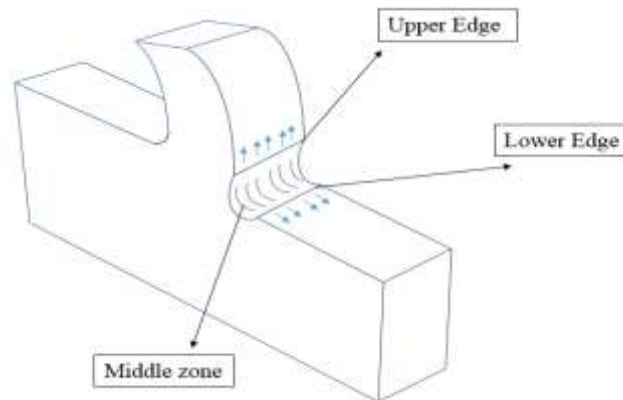


Fig 24) different zones of the chip root

2.6.3 VMG cutting inserts

Tools with uniform cutting edge radius are common, as they are easier to manufacture, however, in some conditions, a uniform cutting edge could have an adverse effect on cutting forces, temperature and surface quality, while Variable Microgeometry (VMG) tools can be used instead. In uniform cutting edge, when the ratio of edge radius to uncut chip thickness decreases, friction increases and the plowing effect will be more dominant than cutting, which could result in higher cutting energy consumption and, because of higher plastic strain, temperature will be increased which, in turn, leads to faster tool wear. As can be seen in Fig 25, with a uniform constant edge radius, at the leading cutting edge (section A-A), the edge radius is smaller than the uncut chip thickness when normal cutting happens, then at the section B-B corner the radius is almost the same as the uncut chip

thickness which causes rubbing of the surface instead of cutting, and, finally, at section C-C where the corner radius is larger than the uncut chip thickness, plowing is unavoidable [30]. Using a variable microgeometry, even at the trailing cutting edge, where material is trapped, a smaller edge radius with regards to the uncut chip thickness, plowing could be avoided.

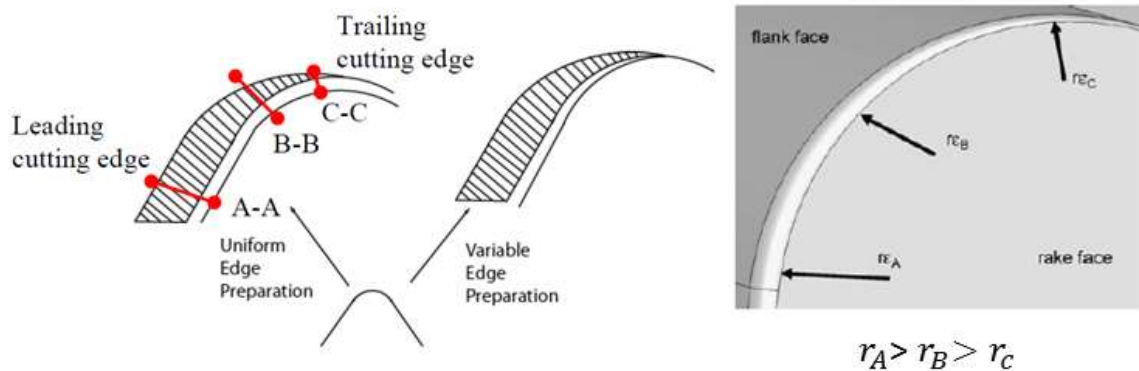


Fig 25) Comparison between conventional microgeometry and variable microgeometry [31]

Karpat and Srivastava [31] conducted a study on four various inserts (waterfall, honed, chamfered and variable microgeometry (VMG)) in the same cutting condition to cut AISI 4340. Temperature and cutting forces generated for these cutting inserts were measured. As expected, VMG cutting insert temperature distribution showed lower values than the others due to a more stabilized ratio of edge radius to uncut chip thickness. Fig 26.

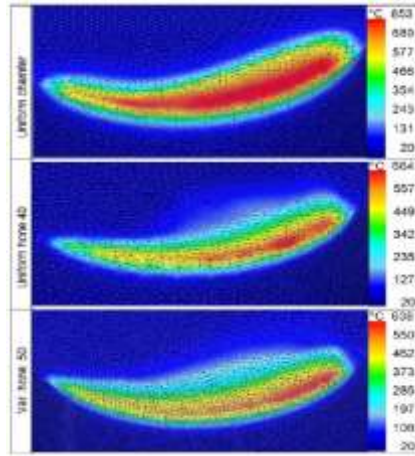


Fig 26) Temperature distribution for uniform and variable microgeometry tool [31]

2.7 Tool Wear

In any material removal process, tool wear is an inevitable phenomenon, which can be due to high temperatures such as those experienced when machining workpiece materials such as low thermal conductive materials like titanium, etc. Thus, to have an efficient cutting process with high productivity, one should consider all parameters which can cause tool failure. It has been shown that when two materials are in contact with each other, the following equation can be applied:

$$\frac{B}{L} = kA_R \quad (39)$$

Where B is the wear volume, L is the sliding length, k is the probability of wear particle formation and A_R is the real contact area. Burwell and Strang [32] justified this relationship using a pin and disk setup. In this experiment a preloaded soft pin was mounted in a stationary position on a rotary disk. This test characterized the wear volume for different

sliding lengths. Also by knowing Eq (39) and plugging it into Eq (40) the following relationships can be formed:

$$P = A_R \cdot H \quad (40)$$

$$\frac{B}{PL} = \frac{k}{H} \quad (41)$$

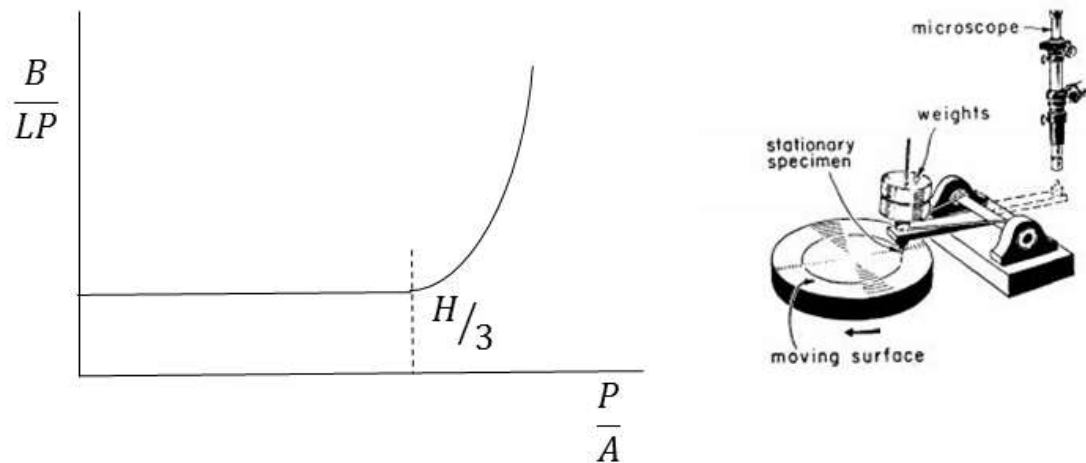


Fig 27) Pin and disk friction test by Burwell and Strang [32]

H is the hardness of material and P is the applied normal load on the pin. The ratio of K/H is constant for a pair of materials in contact until where A_R and wear rate does have an abrupt change.[8] This location was where the ratio of P/A reaches H/3 in the Burwell test. This value (H/3) corresponds to the yield stress of the tool. To explain more clearly, it is better to refer to Fig 28, in the initial period, as a brand new tool is sharp and the contact area is very small, the ratio of force over area might be large enough to reach its yield stress and thus results in rapid tool wear, so the dominant wear mechanism here is more related to plastic deformation and depends on the tool/work pair and cutting conditions. In the second region the aforementioned ratio is less or at maximum close to the yield point, so in

this region other wear mechanisms are prevalent. In the failure region as thermal softening will happen, the value of yield strength might lessen and this in turn results in an accelerating tool wear rate until the point where final failure happens. The final value is different case by case, however, conventionally if the flank wear reaches 300 μm , it technically is the end of tool life.

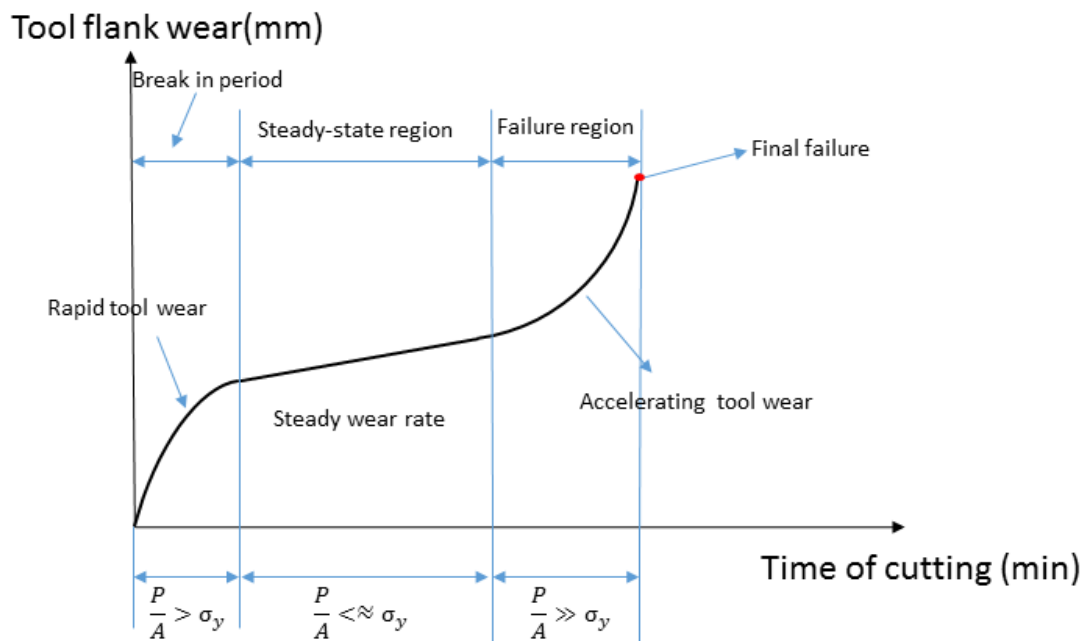


Fig 28) Tool wear curve regions

2.7.1 Flank Wear

As its name suggests this kind of wear occurs on the flank face close to the machined surface. Generally, this type of wear is more of interest compared to crater wear, since the width of the flank wear is more evident and this facilitates the wear measurement under optical microscopes. This type of wear not only affects the tool life, it also has an adverse

effect on the quality of the machined surface and its dimensional accuracy by increasing surface roughness as it is more in contact with the workpiece. When the worn flank face rubs the machined surface, it leads to a rise in the normal load (feed forces). Moreover, due to high friction between the tool and the machined surface, the temperature will increase as well which in turn leads to tensile residual stresses in the surface, which is not favorable.

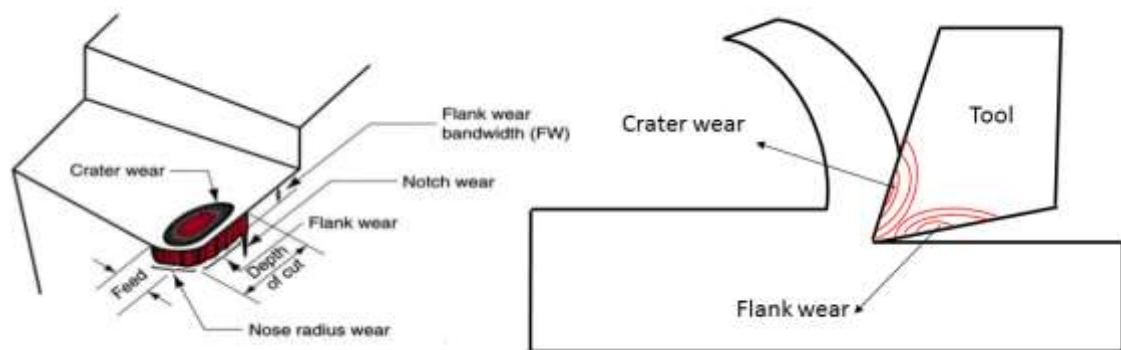


Fig 29) Flank wear vs. crater wear

2.7.2 Crater wear

Although the area of the crater wear is more visible, the maximum depth of crater wear is the parameter that continuously changes during the cut, so this is more of interest for measurement, however, it is rather difficult to measure. This type of wear is normally not harmful for the workpiece and even sometimes larger crater wear could work as a chip breaker and facilitate chip curling, however, as it progresses it makes the tool weaker and weaker until catastrophic failure occurs through large crack formation. As can be seen in Fig 30, in the plunging test that has been performed in this study, crater wear was more evident, while flank wear was used to follow tool wear evolution since the difficulty of measuring crater wear still exists.



Fig 30) Crater wear

2.8 Tool wear Mechanisms

There are six major tool wear mechanisms that depend on cutting conditions; one or a combination of wear mechanisms could occur during the cutting process. Li [33] showed at low speeds, which implies low temperatures, the dominant wear mechanism is abrasion and adhesion, but as cutting conditions gets more severe, such as those experienced under a higher cutting speed, feed, oxidation and diffusion become more prominent. Fig 31 shows that under high cutting speed conditions (high temperature), the probability of adhesion is negligible.

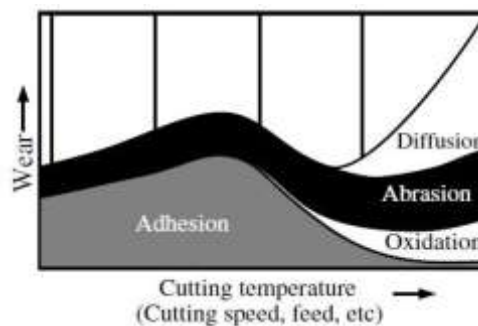


Fig 31) tool wear mechanisms vs temperature and cutting speed [33]

2.8.1 Adhesion

This type of wear is caused by welding of workpiece materials to the surface asperities on both the flank and rake faces of the tool. As the material flows along these two tool faces these welded materials abruptly break off. This can cause fragments of the tool to break off. The wear volume of this type of wear is not necessarily large but it progresses over time to break down the edge of the tool.

2.8.2 Abrasion

Generally, when abrasive particles such as sand and silicon inclusions are present in the workpiece material composition, abrasion can cause severe damage, mostly on the flank face of the tool.

2.8.3 Diffusion

This type of wear mechanism pertains to material diffusion with atoms migrating from regions of high concentration to low. For example, if low-carbon steel were to be cut by a diamond tool or diamond coated tool the carbon in the diamond will diffuse at high temperature and load into the low carbon steel, this transfer of carbon to the workpiece will result in diffusion wear in the surface of the tool breaking down the cutting edge and generating crater wear in the region of highest temperature on the tool. Elevated temperature is the main reason for diffusion wear. Further, as the material flow velocity of the chip near the edge of the tool is very low so materials will have enough time for atom exchange at high temperatures.

2.8.4 Oxidation

When the cutting process performs at a constant depth of cut, the cutting tool includes two portions: The portion where the tool engages with the workpiece constantly, and the free surface that is exposed to the oxygen in the atmosphere which causes oxidation which is accelerated at high temperatures. The wear that is caused by this mechanism is called notch wear. Also the location of notch wear lines up with the depth of cut. Notch wear is tractable if appropriate strategies are applied. Taper cutting is one solution that can provide a variable depth of cut to avoid notch wear.

2.8.5 Fatigue

There are some cases in which fluctuation of thermal or mechanical load due to cyclic load causes cracks on the tool, such as intermittent cutting (milling), various feed and cutting speed. Also cyclic cooling and heating, and selection of wrong exit and entry angle can also impose high thermal and mechanical loads on the cutting edge [34].

2.8.6 Plastic Deformation

In this phenomenon because of high thermal and mechanical load, the tool surface plastically deformed which mostly occurs at the initial step of tool wear where tool edge is sharp and the stress concentration on the tool edge can exceed the tool yield stress. Plastic deformation on the cutting edge in advanced stages can result in edge chipping, which means large fragments of the cutting tool can be broken away.

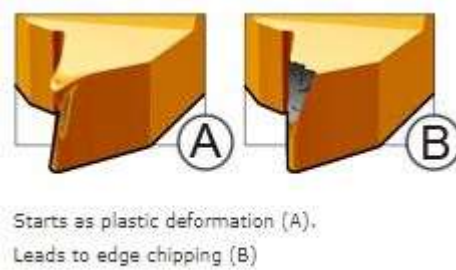


Fig 32) Plastic deformation and edge chipping [Sandvik]

2.9 Edge Preparation

As discussed briefly in the cutting tool geometry section, edge preparation is a mechanical process which removes burrs, defects, sharp spots and any cutting edge irregularities on a tool. This process provides a more uniform cutting edge surface, which helps the coating layer to be deposited with better quality, also it can prevent tool chipping and plastic deformation in early stages. As Denkena and Biermann [19] reported, edge preparation methods, which are commonly used in industry include wet and dry abrasive jet machining where a pressurized jet of abrasive materials is sprayed on the tool edge. Brushing of the edge as Zarif [35] mentioned is a widespread method also used for edge honing. In these methods nylon or wire brushes are used. Nylon brushes are normally impregnated with abrasive particles and are found to work effectively at rounding the edge. Also by changing time, depth of cut and angle of engagement, different edge shapes can be obtained. This preparation method has been used in this research for edge preparation, Fig 33. In contrast with abrasive jet methods, in the drag finishing method cutting tools rotating in a stationary container full of abrasive particles. In this case the accuracy of the resultant geometry features could be determined by process time, speed of rotation and direction of

rotation. Grinding has also been used for a long time to produce a chamfer on the cutting edge. The advantage of this method is that the whole preparation process can be done in one setup together with tool grinding, although the application of grinding in this case is limited to non-complex geometries. In addition the wet and dry abrasive jet method has been found to increase the toughness of the tool by increasing the compressive residual stress in the surface of the tool and fill in micro cracks in the surface of the tool. In this process a jet of abrasive particles with or without liquid is pointed on the cutting edge and performs material removal. In wet and dry abrasive jet processes, the material removal rate (MRR) could be controlled by changing the carrier medium velocity, which could be pressurized water in wet and pressurized air in the dry abrasive jets [19]. There are some other parameters such as feed speed, jet spray angle, jet inclination angle, etc. which affect the final shape of the cutting edge. For example, increasing the feed speed will reduce the impact time which in turn reduces the MRR. Also, higher pressure means that the abrasive particles should move faster in the nozzle and this corresponds to higher MRR.



Fig 33) Sinjet Edge honing machine

Drag finishing is a recommended edge preparation method for symmetrical applications such as drill bits, milling heads, etc. due to the full contact with the small grains and their ability to move around an edge and produce a complex geometry. However, due to full immersion of the cutting edge, it can be a very time consuming process to reach a desirable geometry. In Fig 34, the performance of cutting insert as a result of different edge preparation methods can be seen.

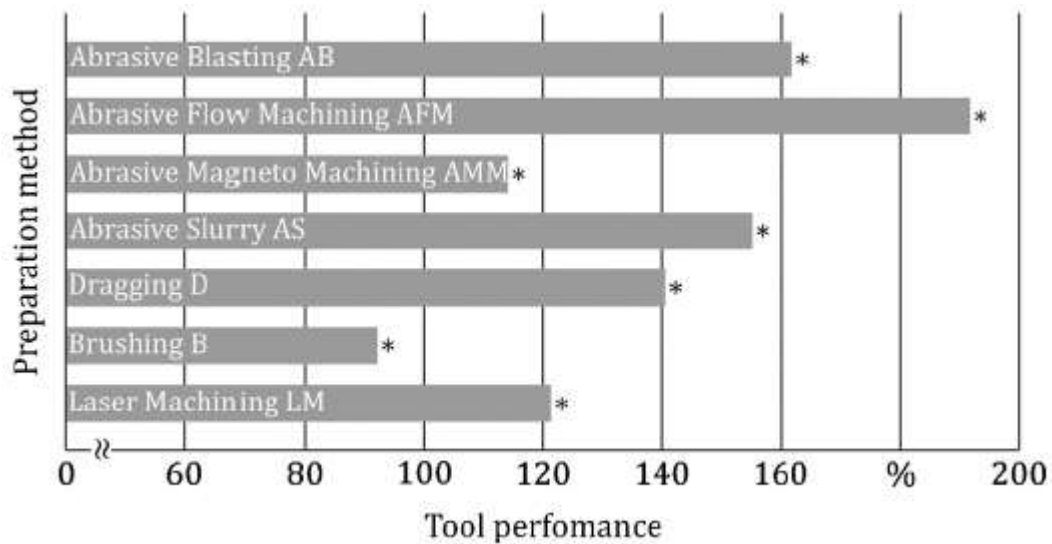


Fig 34) Tool Performance vs. Preparation method [19]

2.10 Friction in machining

Friction is an unavoidable phenomenon between two surfaces with non-zero relative motion. The sources of friction could be an interlocking of surface asperities or micro welding of surface asperities to one another. Due to surface imperfections perfect surface contact area (A_a) between two surfaces rarely occurs, in reality this area is less than 0.01% of the whole surface (A_r) and this is because asperity peaks are the only regions which make

contact. As the normal load is applied, these peaks will be flattened, which results in a greater real contact area (A_r). Shaw [8] provided the graph of shear strength vs. normal stress, Fig 35. As can be seen, this curve consists of three regimes. Regime I illustrates a linear relationship between σ and τ . Since the normal load is light such that $A_a \ll A_R$ then Amonton's law can be applied and within a range increasing the amount of normal load the coefficient of friction will linearly increase. While in Regime II, a logarithmic behavior of COF can be observed. This is because the plastic deformation of the asperities start to overweigh the sliding friction, also the real area (A_r) starts to approach to (A_a). In the last regime, these variations will be stabilized, as the sliding speed reaches to its minimum values such that the two blocks are effectively starting to weld to each other; friction welding is an extreme example of this phenomenon and is used to join two surfaces in special applications. In this case, COF will be independent of the normal load, which is the so called sticking zone and the apparent area and the real area are almost the same.

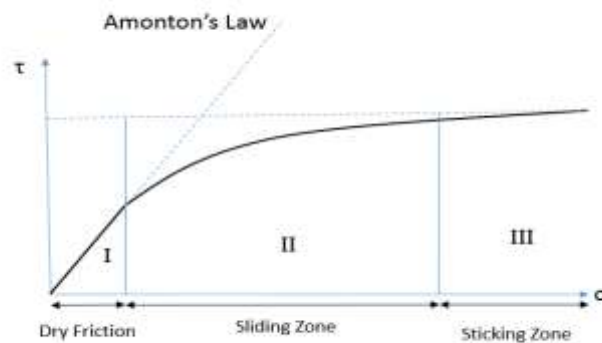


Fig 35) Regions of Solid friction

Classical friction law could be applied for most of the physical phenomenon as long as they occur in one speed direction. For a perfectly sharp tool classical friction laws are valid. However, the reason that classical friction laws are hard to apply in real machining experiments is that, practically there is no perfectly sharp tool. Consequently the chip flows in two different directions around the cutting edge making it difficult to measure the friction force using a dynamometer.

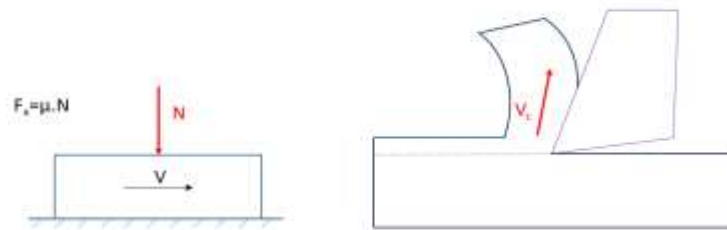


Fig 36) Classical friction law applies for one-direction speed

2.11 Coating

During machining a cutting tool is exposed to both high mechanical and thermal loads which can lead to rapid tool wear even in early stages. An appropriate coating which provides anti-friction, thermal barrier and wear resistant layers can provide for higher tool longevity and better final product surface integrity. Considering a coated tool whose substrate sustains much lower stress compared to an uncoated sharp tool which sustains a high amount of equivalent stress and is already larger than its yield stress. This leads to the formation of micro cracks and chipping on the tool edge [36]. As [37] mentioned, coatings

can be designed to reduce the transmission of heat to the tool, based on two mechanisms 1- It reduces the tool chip contact length (l_f) so as the area of heat transfer is reduced and thus heat transfer in the second shear deformation zone will be reduced. Also 2- the coating layer can operate as a thermal barrier, which again reduces the heat flux. Rech [37] demonstrated this idea by comparing the performance of three different coating layers with an uncoated tool. EDS curves exhibit that thick layers of iron on the uncoated tool rake face were much greater than coated ones which attributed to larger contact area and higher friction in the uncoated tools. This can be justified by the theory of metal cutting as well. The larger contact area, corresponds to the bigger β (friction angle) which results in larger COF. In soft coating as Eq (42) shows the coefficient of friction is dependent on the shear stress and yield stress, as both these parameters in one material normally work in the same direction. So by applying a soft coating layer a low shear strength region and high yield strength is provided by the workpiece material.

$$\mu = \frac{\tau}{\sigma_y} \quad (42)$$

There are two commonly used methods for applying coatings on cutting tools which will be explained here:

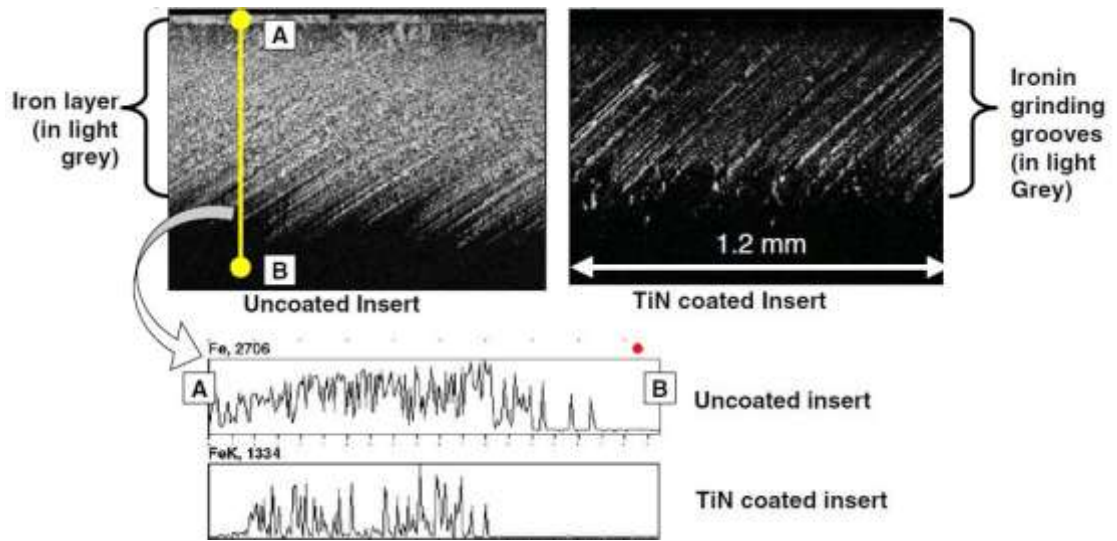


Fig 37) Comparison between uncoated and TiN coated insert [37]

2.11.1 CVD Coating

Chemical vapor deposition (CVD) as its name suggests, is a chemical reaction between two reactants which both are in the gas (vapor) phase. Basically, material is being coated in a vacuum chamber where gaseous reactants enter to this chamber and after reaction together and with workpiece surface atoms are depositing on the workpiece surface. This reaction occurs at high temperature, and then excess gaseous atoms and initiators which speed up the process will be vacuumed out, and this cycle continues until the desired thickness of coating is achieved. The working temperature of CVD (800-1200°C) is higher than Physical Vapour deposition (PVD)(300-400°C) which is discussed in the next section as is the thickness layer (10-200 μm versus 2-5 μm for traditional PVD) as mentioned by Davim [38]. These high temperatures can impose metallurgical limits for the materials such as cemented carbide which cannot withstand these high temperatures [39]. However, this type of coating method is able to deposit multi-layer coatings on the tool. For example, a

multi-layered TiC+ TiCN+Al₂O₃, covered by a CVD which can protect the brittle Al₂O₃ from damage specially in the first stage of tool wear [39].

2.11.2 PVD Coating

In physical vapor deposition (PVD) again a relatively high temperature, and high vacuum chamber is needed, however, in this process a piece of metal referred to as the target which includes elements which are to be coated on the surface (such as Titanium) is evaporated by a plasma arc and then after reacting with hot reactive gases (such as Nitrogen) is deposited as a layer on the surface of a tool (TiN). This kind of coating is very smooth and thin, normally less than 5 μm. Also the working temperature is much lower than CVD, and varies from (150 - 500°C). The advantage of PVD is the wide range of coating materials and substrates that can be used. Metals, alloys and ceramics can be deposited on a wide range of metals, ceramics and even paper and plastic. Moreover, because of the nature of the process, this method provides a very adherent coating layer and the microstructure of the coating can be tuned by manipulating the coating parameters. TiN and TiAlN are prevalent coating materials applied to cutting inserts and milling tools. Although CVD coating provides thicker coatings they are limited in terms of the materials that can be deposited. Also as CVD coatings have a high level of tensile residual stresses, they are not recommended for use in intermittent cutting operations such as milling [39]. Today, there are some hybrid methods which combine the advantages of both CVD and PVD coating methods together.

2.12 Stress flow

The value of stress at each specific strain which material can sustain and plastically flow prior to any failure, rupture or fracture, can be referred to as flow stress. This also corresponds to material behavior under plastic deformation circumstances. It has been very controversial to find a unique governing equation which is able to cover all of the affecting parameters on the flow stress model in machining due to the high order of strain and strain rates. So it is very difficult to find a governing equation which consider all governing mechanism of machining which means that during the cutting operation some of the mechanisms dominate. As described in earlier sections, machining is an aggressive and harsh physical and chemical process due to large deformation, high level of strain and strain rates and normal stresses. Based on the literature, Johnson-Cook constitutive plastic model has been largely used in machining due to the fact it includes aspects critical to machining such as strain rate, strain hardening and thermal softening effects [14], [40]–[48]. Thus, this comprehensive plastic model has been used in the models developed in this thesis and will be discussed in the material model section.

2.13 Damage Models

In ductile failure, material sustains plastic deformation up to the point at which it loses its load carrying capacity and fracture occurs. There are a number of ductile fracture models which have been used to model the material removal process as mentioned by [49]. As can be seen in Fig 38, in ductile materials, normally damage initiates where necking happens at (damage parameter, $D=0$) when material still keep the same modulus of elasticity, by increasing the (D) material approximates to complete failure at $D=1$ where

failure occurs. In the Johnson-Cook material model the damage parameter D can be calculated by the following equation:

$$D = \frac{\sum \Delta \bar{\varepsilon}_{pl}}{\bar{\varepsilon}_f^{pl}} \quad (43)$$

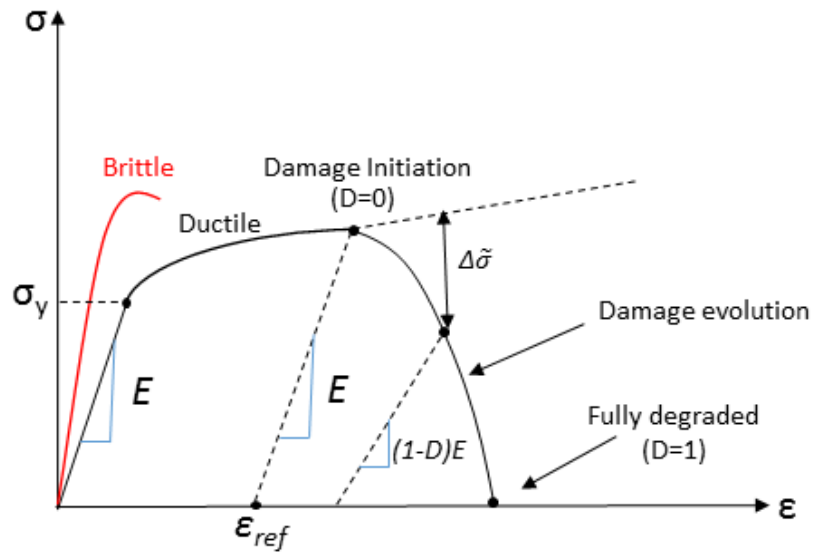


Fig 38) Ductile fracture stress-strain curve

If D exceeds unity, fracture in the material occurs, where $\Delta \bar{\varepsilon}_{pl}$ the calculated equivalent plastic strain in each time step and $\bar{\varepsilon}_f^{pl}$ is fracture plastic strain obtained from Eq (45). Liu et.al [50] compared six different damage criteria including: constant fracture strain, Johnson-Cook, Johnson-Cook coupling criterion, Wilkins, modified Cockcroft-Latham, and Bao-Wierzbicki fracture. They mentioned the Bao-Wierzbicki (B-W) fracture model which is a relatively new fracture model but has been applied to machining and showed the best performance in terms of prediction while including the effect of strain rate dependency,

temperature and damage evolution, however, the disadvantage of this model is that finding fracture parameters for this model needs numerous experiments, so they are difficult to obtain. Johnson-Cook with coupling criterion was also relatively accurate at predicting cutting forces, temperature, stress flow, and also surface roughness accurately. The only deficiency of the pure J-C damage model is its inability to predict accurate chip formation and cutting forces due to the unrealistic damage prediction for stress triaxiality smaller than -0.33. As discovered by Bao and Wierzbicki [51] the cut off value is the threshold value before which no material failure occurs. However, this issue for the pure Johnson-cook is compensated by its ease of implementation as compared to other models which is considered to be one of the advantages of this model [52]. As can be seen in Fig 39, Bao-Wierzbicki model includes three branches and can predict fracture strain in a wider range of stress triaxiality [53], so B-W is a more accurate model in terms of chip morphology and cutting force prediction. However, it requires several fracture parameters, some of which are difficult to determine from experiments as reported by Bao and Wierzbicki [49]. As shown in Fig 39, B-W fracture could be a result of shear, compression, or tension depending on the value of stress triaxiality. In this research, tensile fracture is the dominant fracture mechanism which will be discussed in detail in the modeling section.

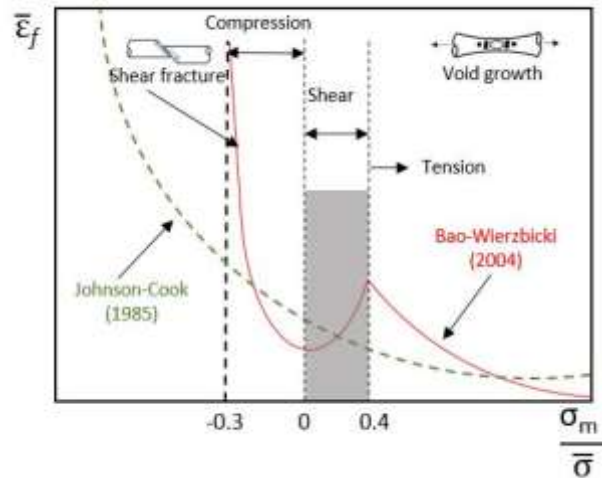


Fig 39) Fracture locus for AL 2024-T351 [53]

2.14 Failure Criteria Models

The basic idea in machining is that when the tool tip engages with the work material, it tries to tear off the work material physically with minimum consumed energy and then the separated material flows along the tool rake face to form a chip which then curls and detaches. In this regard, researchers have defined different failure criteria to model machining process. Some of these models will be discussed here.

2.14.1 Element Failure Criteria

This phenomenon is simulated in the Lagrangian model by dividing the workpiece into three layers. The top one is called the chip layer, the sacrificial layer is in the middle and the bottom layer which is in contact with the tool is called the machined surface and at the bottom is fixed spatially. Establishing a meaningful failure criteria have been studied by many researchers and they have come up with some new ideas. Usui and Shirakashi [2]

pioneered a failure method based on the distance between the tool tip and the closest point along the machined surface, so when this distance becomes small enough separation occurs. As Shaw [8] reported most of these criteria operate in accordance with their limit values. For example, Carroll and Strenkowski [54] proposed the same criteria as Usui and Shirakashi [2] but used strain as the determinative factor. Lin [55], studied strain energy as a criteria for chip separation, Iwata et al. [3] picked a ductile fracture criteria, and Cereti [56] and Zhang et al.[57] used a critical damage value and fracture mechanics respectively. Although, in the primary shear deformation zone (PSDZ) the dominant mechanism of deformation is a combination of shear and compression, the real mechanism for failure ahead of the tool is tension. Thus, element failure occurs through the sacrificial layer and failure parameters that have been defined for this layer. When the tool forms the chip, the elements ahead of the tool start to stretch and when their displacements hit the maximum value defined in the software, those elements are automatically removed, as shown in Fig 40. So that is why in this study, tensile fracture has been considered as a failure mechanism. Also Johnson-Cook parameters which were used in this study have been exported from a tensile test done by [58]. The main disadvantage of this method is element deletion, which is a non-physical process and leads to mass density reduction, and consequently it can affect the cutting force results, this is mentioned by Zetterberg [59]. So in order to minimize this adverse effect, the sacrificial layer thickness should be as small as possible and a very fine mesh density is advised to avoid large mass reduction which directly can affect the calculation of the matrices.

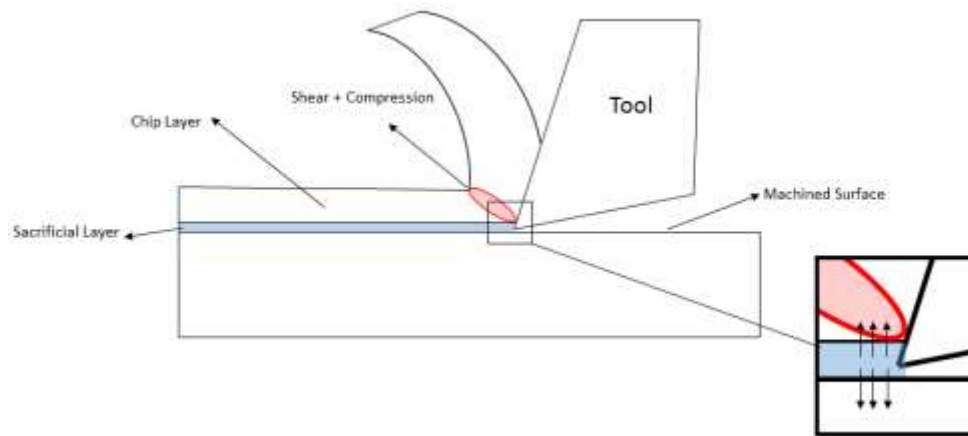


Fig 40) A schematic of Lagrangian model with tensile damage failure

2.14.2 Meshless Methods

As its name suggests in these kind of models problems are not segmented to elements but to a huge number of particles which is accomplished by a process called The Particle Finite Element Method (PFEM). In other words, this method modifies the problem to a mass of particles instead of elements, and each particle has its own cinematic and dynamic characteristics and material properties based on its mass, internal and external forces. Thus the resultant force applied to each particle is the result of interaction between that particle and its neighbors [60]. The aggregation of these calculation for all particles is the final solution.

3. Modeling

Although there are extensive number of complex cutting operations which in the first sight are challenging to model, at small scales orthogonal cutting theory can be applied to

most of them. Thus, in this study, a 2D coupled thermo-mechanical model was developed by using ABAQUS CAE/ 6.14-2 to capture cutting forces, temperature profile and stresses, which are vital factors that affect tool life. To develop this model a Coupled Temperature-Displacement Dynamic/Explicit solver method has been used.

3.1 Modeling Formulations

Basically, in the finite element method, a complex problem can be split into a large number of elements and nodes, so instead of solving the whole complex part at once, these finite nodes are analyzed by parallel equations mechanically and thermally and then they are aggregated to find the final solution. The more elements cover the whole body, the more accurate the result is going to be. However, as we know, there is a trade-off between calculation time and accuracy. Metal cutting simulation has been one the most challenging modeling problems due to the large deformation, high level of strain and strain rates. There are three main formulations which are commonly used for modeling of material removal: Lagrangian, Eulerian and Arbitrary Lagrangian Eulerian (ALE).

3.1.1 Lagrangian

Lagrangian is a classic and fairly accurate FE formulation which is able to predict the material behavior from the very beginning of cutting so knowledge of geometrical features such as tool chip contact length, chip shape, etc. beforehand are not required for simulation like other types of formulations. In this manner, elements are attached to the material, so material deformation corresponds to element deformation and as mentioned large

deformation and large strain and strain rate are inevitable in metal cutting, mesh distortion is a common issue in this type of formulation.

3.1.2 Eulerian

In the Eulerian formulation, elements are fixed spatially, and as the material flows through this control volume, mesh distortion can be avoided. Also, a smaller number of elements is required, thereby the calculation time will be reduced. However, in this method, initial chip shape, tool chip contact and shear angle must be known prior to any simulation, also the chip is not formed based on an element separation mechanism which makes this method not effective for modeling metal cutting [61].

3.1.3 Arbitrary Lagrangian Eulerian (ALE)

ALE is a hybrid method which combines the advantages of both Lagrangian and Eulerian, in which elements are neither attached to the material (Lagrangian), nor fixed spatially (Eulerian) [61]. In this method, typically the tool is fixed and the workpiece is movable and the idea is splitting the workpiece into an Eulerian part which is adjacent to the tool tip where the largest deformation happens to avoid mesh distortion and no need for re-meshing, while the rest of the regions including the free boundaries will be analyzed by Lagrangian elements. This allows the chip to flow and curl freely, so that the tool chip contact can be extracted from the model [62].

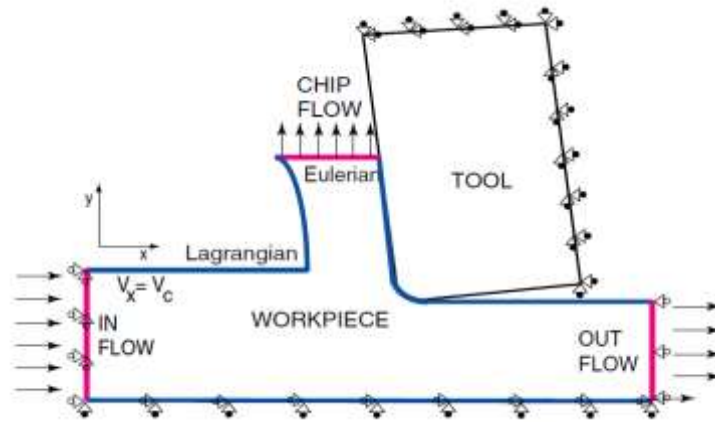


Fig 41) ALE formulation [26]

3.2 Methodology

An updated Lagrangian formulation was chosen for this study because of its simplicity and accuracy compare to others as mentioned before. Also the Lagrangian formulation is the only model which applies a fracture criterion to predict the element failure which reinforces its predictability and leads to the generation of reasonable data. While the others benefit from non-physical damage criteria like the Eulerian method [52]. Re-meshing and pre-distorted method are prevalent solutions to come up with large element distortion. In the first method one algorithm tries to find distorted elements and reshape them in order to proceed the modeling. In the second one, which is the method used in this research, elements in the workpiece top layer (chip layer) are tilted by an angle which is not creating any acute angle less than 10 degree and obtuse angle larger than 150 degree in any elements, as advised by the ABAQUS 6-14 user manual [63]. The reason for that is, in metal cutting especially for the tools with zero or high negative rake angle, the cutting tool imposes a large amount of compressive stresses on the workpiece elements and can cause severe mesh

distortion. So the un-deformed elements start to be crushed and stretched severely, so the elements will be completely devastated and it can abort the simulation even in early stages. However, if the elements are pre-distorted a little bit, the shape of that element after deformation will be like an un-deformed one so the final level of distortion will be minimized. Moreover this techniques saves time as remeshing is a very time consuming method, even for simple problems.

3.3 Element Definition

The element type that should be used for this type of modeling should first be 2D plane strain and should capture both the mechanical and thermal loads and properties and because of that, 4-node plane strain thermally coupled quadrilateral, bilinear displacement and temperature, reduced integration, hourglass control (referred to as CPE4RT) is being used to assign both tool and workpiece geometries. As mentioned above, there are two strategies that we can apply to avoid uncontrolled mesh distortion which is a challenge particularly in negative rake angle tools. A pre-distorted CPE4RT element was chosen according to a combined temperature-displacement solver method. In the re-meshing method an algorithm recognizes the distorted elements by node relocation, which leads to the loss of some of the data points instantly which is why in this study the other method has been used, also it is very time consuming. In order to have a more effective use of elements, Quad structured elements have been used for the chip layer and the sacrificial layer. However, for lower parts of the workpiece the free mesh was used and also the density of the elements has been reduced as having a high accuracy on that part is not required. The number of elements on the cutting insert was large, with more concentration towards to tool tip from both the rake

and flank face. Cutting tool was 5 mm in height and 3mm in width. Fig 42, illustrates the number of elements which have been used in the simulations.

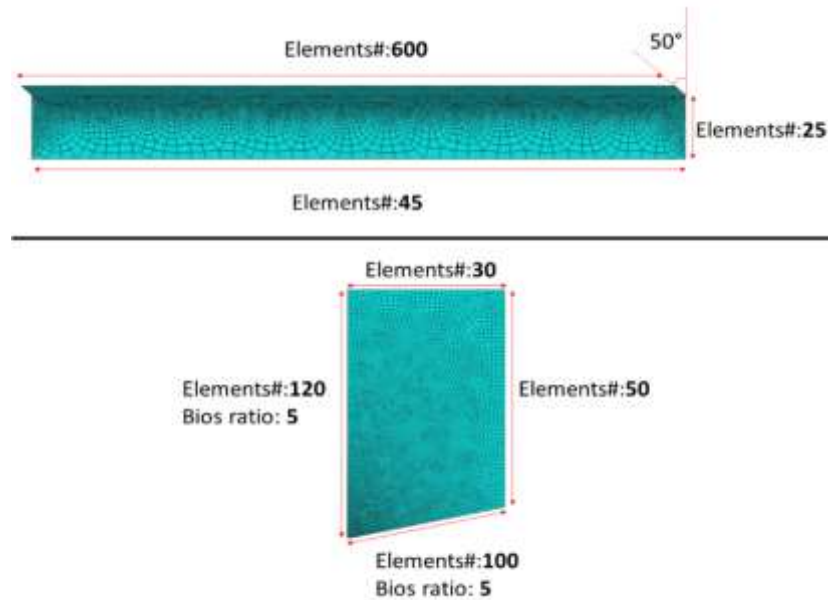


Fig 42) Number of used elements for tool and workpiece

3.4 Material Model

The workpiece material modelled was AISI 1045 with a chemical composition by weight of 0.42% C, 0.17% Si, 0.5% Mn, 0.3% Ni, 0.25% Cu and balance Fe. The material was annealed at 650°C for two hours followed by controlled cooling to room temperature, which resulted in a yield tensile strength of 586 MPa. The Johnson-Cook plasticity material model, together with the Johnson-Cook tensile fracture models was used, as detailed in Eq (44) and Eq (45). Wang [58] performed low strain rate uniaxial tensile tests at different temperatures to determine the constants for strain hardening and thermal components as shown in Table 1. The strain rate constant was assumed to be similar to those discovered by

Jaspers [64]. Table 2, details the constant for the Johnson-Cook tensile fracture model. These constants were acquired experimentally by performing a tensile fracture test to investigate the effect of stress concentration and temperature on fracture strain [58]. The effect of the strain rate constant for the fracture model was assumed to be 0.002 [65].

$$\sigma_{pl} = \underbrace{[A + B\varepsilon^n]}_{\text{Strain hardening effect}} \underbrace{\left[1 + C \ln\left(\frac{\dot{\varepsilon}}{\dot{\varepsilon}_{ref}}\right)\right]}_{\text{Strain rate effect}} \underbrace{\left[1 - \left(\frac{\theta - \theta_{amb}}{\theta_{melt} - \theta_{amb}}\right)^m\right]}_{\text{Thermal softening effect}} \quad (44)$$

$$\varepsilon_f = \left[D_1 + D_2 \exp D_3 \left(\frac{\sigma_{hydrostatic}}{\sigma_{von Mises}} \right) \right] \left[1 + D_4 \ln \dot{\varepsilon} \right] \left[1 + D_5 \left(\frac{\theta - \theta_{amb}}{\theta_{melt} - \theta_{amb}} \right) \right] \quad (45)$$

Table 1) Johnson-Cook plastic parameters

Strain hardening components			Strain-rate components		Thermal components		
A [MPa]	B [MPa]	n (-)	C (-) [64]	$\dot{\varepsilon}_{ref}$ (s ⁻¹)	m (-)	θ_{melt}	θ_{amb}
615.8	667.7	0.255	0.0134	1	1.078	1500	25

Table 2) Johnson-Cook damage parameters

Stress triaxiality components			Strain-rate component	Thermal component
D_1 (-)	D_2 (-)	D_3 (-)	D_4 (-)[65]	D_5 (-)
0.04	1.03	-1.39	0.002	0.46

Where σ_{pl} the plastic flow stress and ε is the plastic strain. The ratio of $\frac{\dot{\varepsilon}}{\dot{\varepsilon}_{ref}}$ is called equivalent plastic strain rate, which is dimensionless, with $\dot{\varepsilon}$ being the plastic strain rate and $\dot{\varepsilon}_{ref}$ is the reference plastic strain rate ($\dot{\varepsilon}_{ref}=1$). $\left(\frac{\theta - \theta_{amb}}{\theta_{melt} - \theta_{amb}}\right)$ represents a dimensionless

temperature, where θ_{amb} and θ_{melt} are ambient and melting temperature respectively. As can be seen, there are three brackets in Eq (44). The first one includes the strain hardening effect, while the second and third ones cover the strain rate and thermal softening effect, respectively. Eq (45) shows the damage criteria which were used in the model. As can be seen, ϵ_f is the equivalent fracture strain and $\frac{\sigma_{hydrostatic}}{\sigma_{von Mises}}$ is the dimensionless pressure-stress ratio called stress triaxiality, where $\sigma_{hydrostatic}$ is the mean value of three normal stress components and $\sigma_{von Mises}$ is the equivalent von Mises stress. D_1 to D_5 are the damage constants which are material dependent and can be exported by fracture test [66]. Mechanical material properties of AISI 1045 in Table 3 and temperature dependent thermal features of the AISI 1045 and carbide tool have been tabulated in Table 4. The uncoated carbide tool material was modelled as elastic with a 560 GPa modulus of elasticity, 0.22 Poisson's ratio, 220 J/kg K specific heat capacity and 14,500 kg/m³ density. The thermal conductivity was a function of temperature, which ranged between 34 to 47 W/mK within 23°C to 1000°C.

Table 3) Mechanical properties of AISI 1045 and carbide insert

Properties	AISI 1045	Uncoated carbide insert
Density (kg/m3)	7870	14500
Young Module (Pa)	2E+11	5.6E+11
Poisson's Ratio	0.3	0.22
Inelastic Heat Fraction	0.9	---

Table 4) Thermal properties of AISI 1045 and Carbide insert

Workpiece(AISI-1045)			Temperature(°C)	Tool(Carbide)	
Conductivity	Expansion Co	Specific Heat		Conductivity2	Expansion Co2
52			0		
	1.01E-05		20	34	5.40E-06
		470	25		
51			100		
	1.20E-05	535	200		5.30E-06
			250	38	
46			300		
	1.30E-05	635	400		5.40E-06
38			500	42	
	1.53E-05	800	600		5.60E-06
30			700		
			750	45	
			800		
			900		
27			1000	47	
			1250	49	

In the Lagrangian method, typically both plastic damage criteria only are assigned to the sacrificial layer where the material failure occurs, while for the rest of the workpiece including the chip layer and the bottom side of the workpiece just plastic deformation will be assigned. The same procedure is followed in this study.

3.5 Boundary conditions

In this research nine explicit simulations have been performed in order to study the effect of edge radius on tool life, chip formation, cutting forces and temperature. These simulations include three different cutting feed rates ($f=0.05$, $f=.01$ and $f=0.2$ mm/rev) with three different edge geometries (10, 20 and 40 μm). The cutting speed was unchanged during all of the simulations at $V=350\text{m/min}$. Modeling was done using the Updated

Lagrangian method which was discussed earlier in this thesis. The challenge of finding the optimum sacrificial layer as discussed in the failure criteria section. From this section, it is clear that one size of sacrificial layer could not work for all situations, particularly as the different corner radius should have been investigated. In machining simulations, the sacrificial layer should be large enough to make sure that the chip layer element failure happens within the sacrificial layer, otherwise the chip layer, after being exposed to high compressive stresses from large edge radius, can start to fail which is an issue as the damage criteria is not defined for it so the simulation will be aborted by the software. Conversely the sacrificial layer should be small enough to avoid a large reduction in the mass element matrices. By looking at the different edge radius geometries and also considering the points that have been mentioned above, the minimum sacrificial layer was obtained as outlined in Fig 43:

Fig 43:

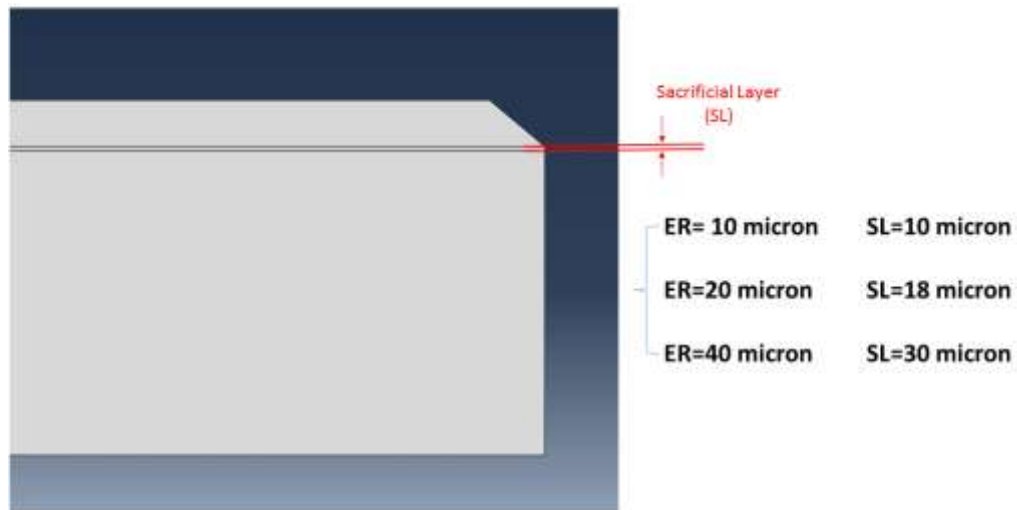
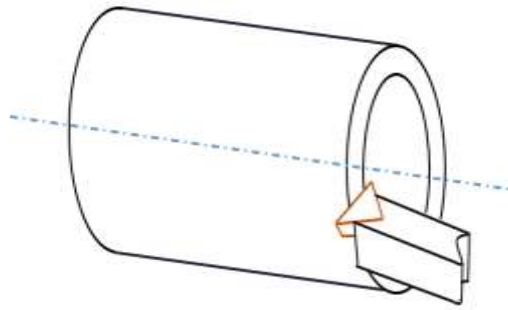


Fig 43) sacrificial layer thickness for each edge radius

The carbide tool was constrained in the x and y direction initially, but then it was freed to move in the x direction at 350 m/min through an AISI 1045 workpiece that is 15 mm in length and 1.5 mm in height. The workpiece was fixed on the bottom side in all directions during cutting. Each simulation dedicated time step was 0.005 sec. in total within 25 increments. The interaction between tool and workpiece was associated with a constant value of friction (0.22), as was used by Wang [58]. Also as discussed before 0.56 of heat is transferred to both chip and workpiece. The width of the cutting tool and workpiece according to the experiments are 12 mm and 3 mm respectively.

4. Experimental Work

As discussed in the simulation chapter, orthogonal cutting makes it easier to simulate the cutting processes, capturing chip formation-related phenomena, temperature profile and cutting forces to name but a few. Also it was mentioned that in reality cutting inserts are exposed to three force components. Thus, in order to replicate orthogonal cutting in experiments, two options exist: 1- Fin cutting (plunging operation) 2-Thin tube turning (turning operation) [44] Fig 44.



a)



b)

Fig 44) a) Thin tube turning, b) Fin cutting

In this research, the plunging process was chosen for two specific reasons: firstly, for thin tube turning experiments, the outer diameter used should be at least 10 times larger than the wall thickness, which causes rigidity issues for the workpiece and introduces a potential for an intense level of chatter and vibration. These vibrations can have an adverse effect on tool life and also force measurements. 2- Secondly, although the cutting length calculation is more difficult in fin cutting as compared to tube turning, fin cutting can be controlled by constant time and number of fins. For the experiments round billets, of AISI 1045 were cleared off by a coated carbide insert to generate a smooth surface. Fig 45 provides an image of the machining setup. Cleaning the surface between cuts was done by a grooving tool with the width of 5 mm as shown in Fig 46. As the cutting insert is very large, the dimensions were defined to ensure that there was enough space during the plunging test on both sides of the fins. Thus, each groove is the result of two overlapped grooving

operations. The whole cutting process was done on a Boehringer VDF180 CM turning centre.



Fig 45) Surface cleaning



Fig 46) Sandvik Coromant grooving tool

The cutting insert which was selected for these experiments was a carbide insert TPGN160302 from Kennametal. In total, nine inserts were used in the experiments including a group of three inserts without any modifications in their geometry with 10 μm edge radius. The other two groups were sent for edge radius preparation. Three of them prepared nominally to 20 μm and the rest set to 40 μm . A used insert is shown in Fig 47.

Each group of experiments was done separately, in order to avoid any inclusion of the other parameters and have consistent experiments for all cutting conditions.



Fig 47) TPGN160302 Kennametal carbide turning insert

The following table shows the experiments that have been done in this study.

Table 5) Experimental work conditions

Feed \ Edge Radius	F= 0.05 (mm/rev)	F= 0.1 (mm/rev)	F= 0.2 (mm/rev)
10 μm	✓	✓	✓
20 μm	✓	✓	✓
40 μm	✓	✓	✓

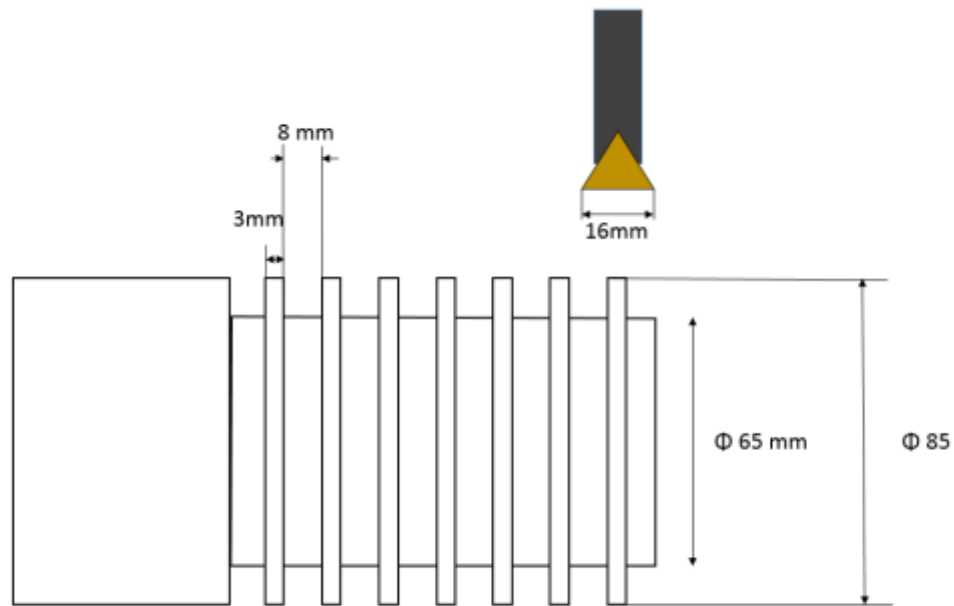


Fig 48) Schematic of plunging test

The cutting and feed forces were measured by a Kistler dynamometer which had three different output channels for force measurements in X, Y and Z directions. These forces were collected through a National Instrument data collection system and transferred to a LabView program installed on a desktop PC. As can be seen in Fig 48, the duration of each experiment is short, as the maximum depth of cut is around 20 mm in diameter in which 2 mm of workpiece diameter was used in order to make sure that the cutting inserts are not touching the root of the fins as this would cause a big jump in the cutting forces and is not consistent with the orthogonal cutting conditions. Then the total 18 mm is divided into three sections, so each time the maximum depth of cut is 6 mm in diameter. This was set to make sure that no major changes in wear occurred during the cutting process.



Fig 49) Kennametal CTCN-443-Plunging tool holder

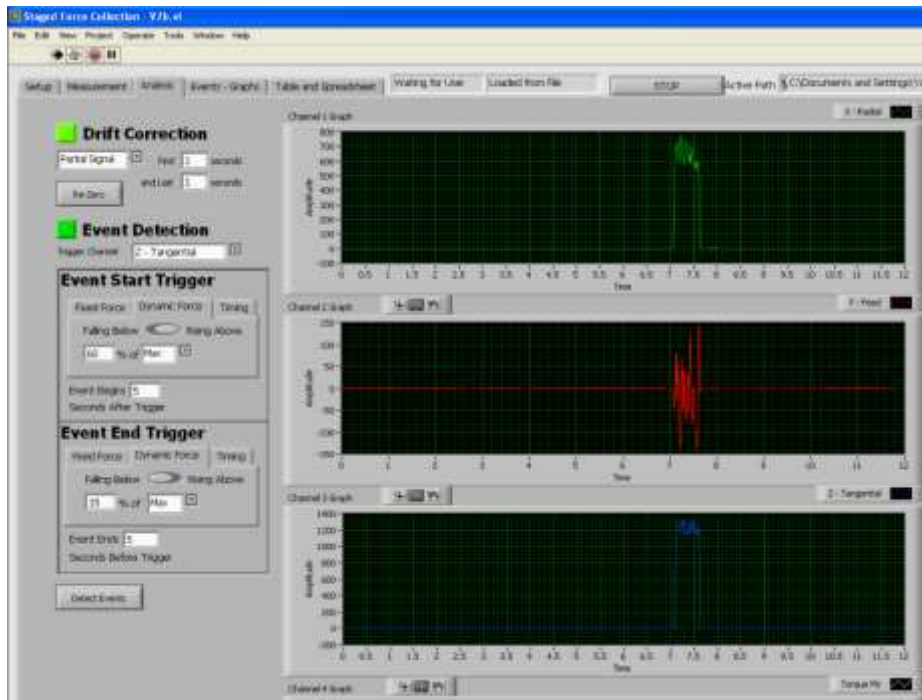


Fig 50) Lab View user interface for force collection

In Fig 50, it is clear that the average of the third component of cutting forces (red colour) is close to zero, which meet the requirements of orthogonal cutting.

4.1 Edge radius measurement by ALICONA

Corner radius of all tool edges were measured using an Alicona Infinite Focus system. Typical edge radius values are shown in Fig 52, Fig 53 and Fig 54. Alicona uses focus variation technology to capture tool edge topography by scanning it and analyzing it using its built in software. This setup is well suited to measuring edge radius and volumetric changes between new and worn tools.

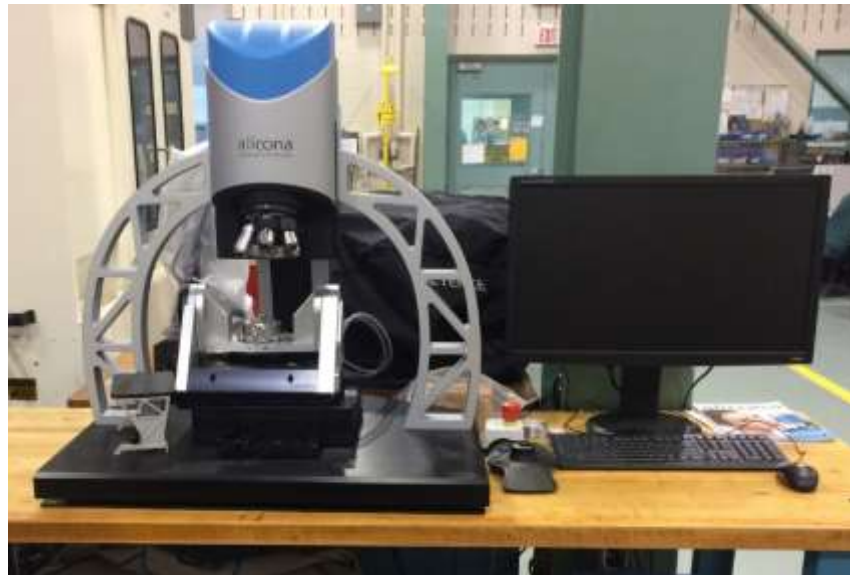


Fig 51) Alicona Infinite Focus G5 Measurement System

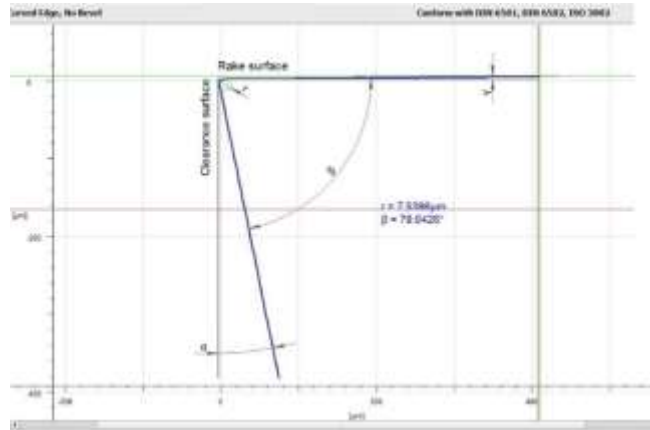


Fig 52) Edge radius measurement- 10 μm

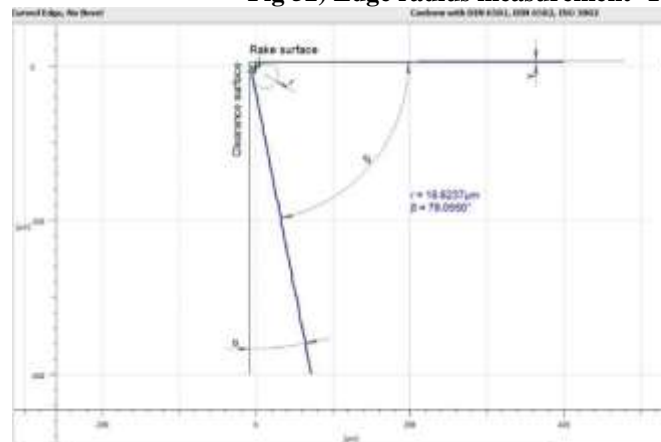


Fig 53) Edge radius measurement- 20 μm

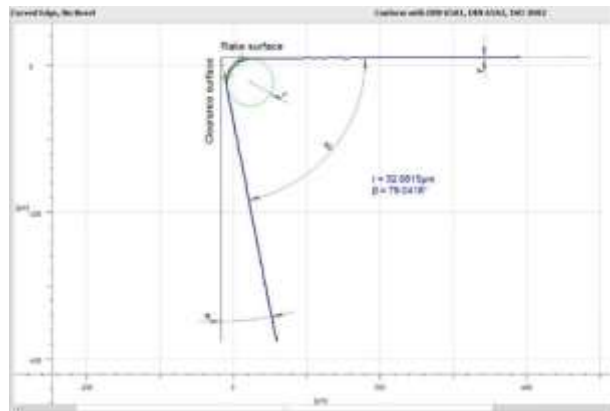


Fig 54) Edge radius measurement- 40 μm

5. Results and Discussion

5.1 Tool wear

The evolution of tool flank wear was studied on tools prepared with three different edge geometries under three different cutting conditions with tool wear evolution monitored intermittently using a KEYENCE VHX-6000 series video microscope as shown in Fig 55.



Fig 55) KEYENCE VHX-6000 video microscope

Fig 56, Fig 57 and Fig 58 provide the tool wear curves for the tools with 10, 20 and 50 μm respectively. The tool life of the tools with the 10 μm and 20 μm edge radius performed similarly, with the 10 μm tool performing slightly better. The tool prepared with the 40 μm edge radius provided the worst tool life by far. The performance of the tools under different cutting conditions will be analyzed further in the following pages.

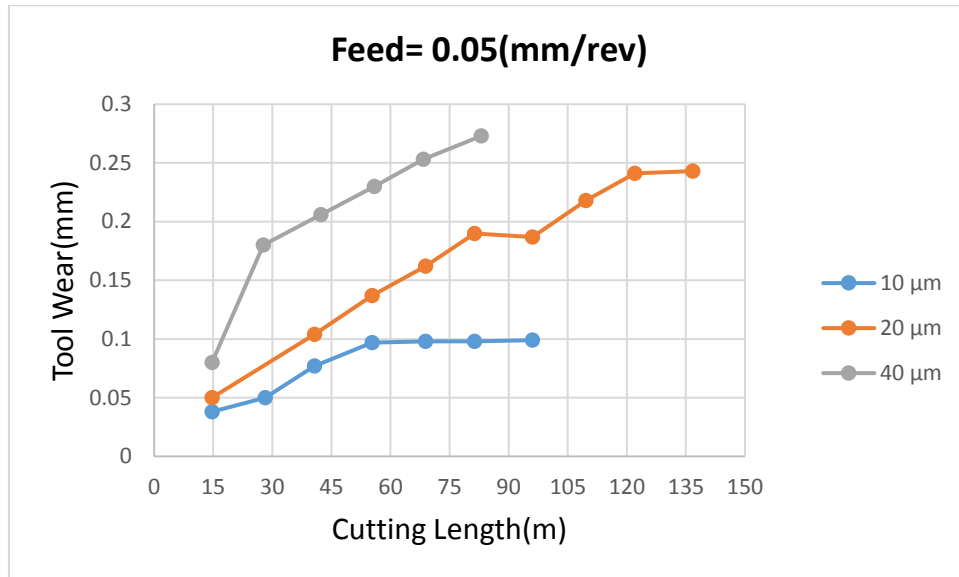


Fig 56) tool wear curve for feed= 0.05 (mm/rev)

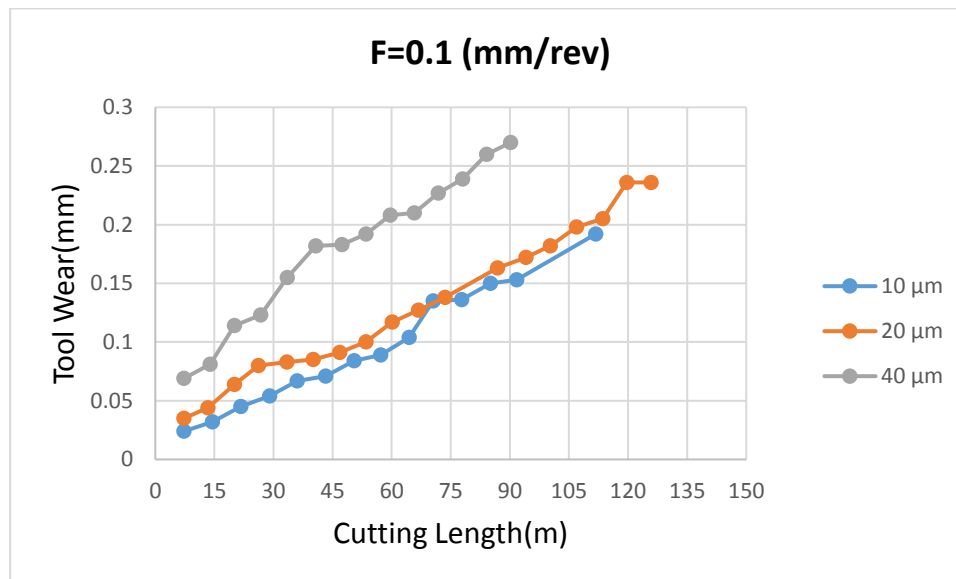


Fig 57) tool wear curve for feed=100 (mm/rev)

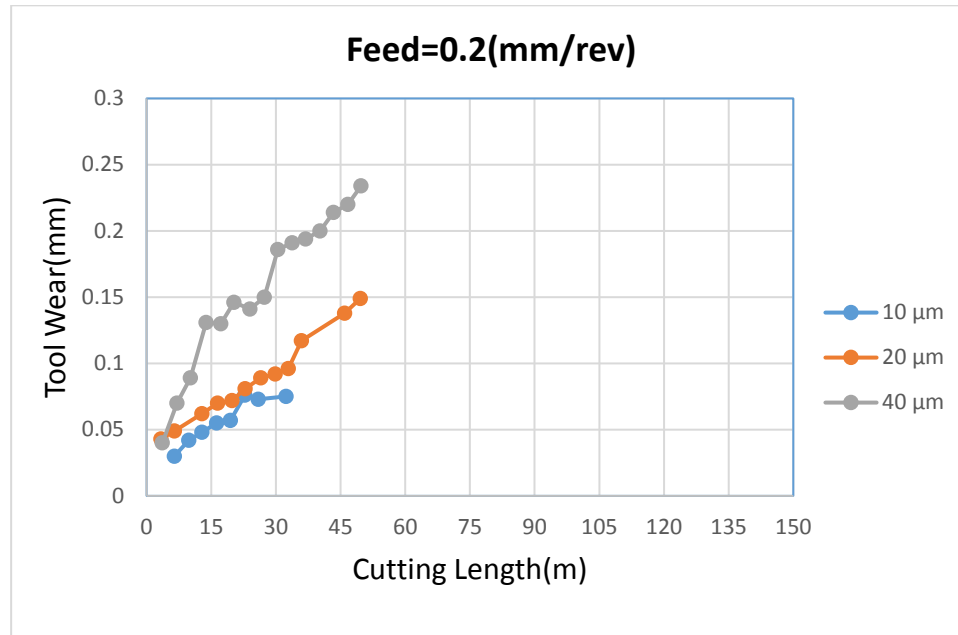


Fig 58) tool wear curve for feed=200(mm/rev)

As the presented model is more applicable in the first step of tool wear where mechanical damage is the dominant tool wear mechanism, data points up to a maximum of 80 μm of flank wear were studied. Fig 59 shows that tool life decreases as edge radius increases and generally as feed rate increases with the exception of the 0.1 mm/rev feed for the 10 μm edge radius tool which provided the longest life.

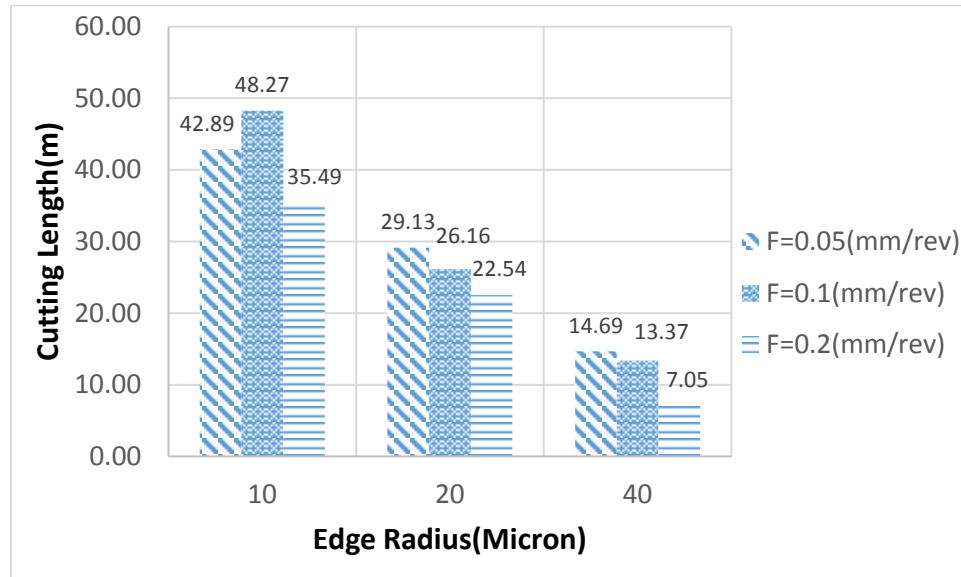


Fig 59) Cutting Length up to 80 μm tool wear

This is supported by Gorczyca (1987) formula for tool life:

$$T = \frac{48.6 * 10^6}{V^4 f^{1.6} d_w^{0.48}} \quad (46)$$

Where v , f and d_w are cutting velocity, feed and depth of cut respectively, which means by increasing cutting feed, tool life should be decreased. However, as mentioned the one exception for the 10 μm edge radius cutting insert at the lowest feed. Astakhov [67] mentioned that there are some situations in which the effect of higher cutting feed can have positive effects on tool life. For example, by increasing cutting feed the level of vibration decreases appreciably due to the increase in rigidity of the machine tool and this in turn increases the tool life. Fig 60, Fig 61 and Fig 62 depict the effect of cutting feed on the force signature with feed rates of 0.05 mm/rev, 0.1 mm/rev and 0.2 mm/rev respectively. As can be observed from Fig 60, the force signatures have a high magnitude of fluctuation

as compared to other feed rates while the difference of this magnitude between 0.1 mm/rev and 0.2 mm/rev is negligible, so as the minimum edge radius does have the lowest contact area with the workpiece, it is not rigid enough and caused vibration at the minimum cutting feed and this in turn caused rapid tool wear compared to the rest of the test conditions.

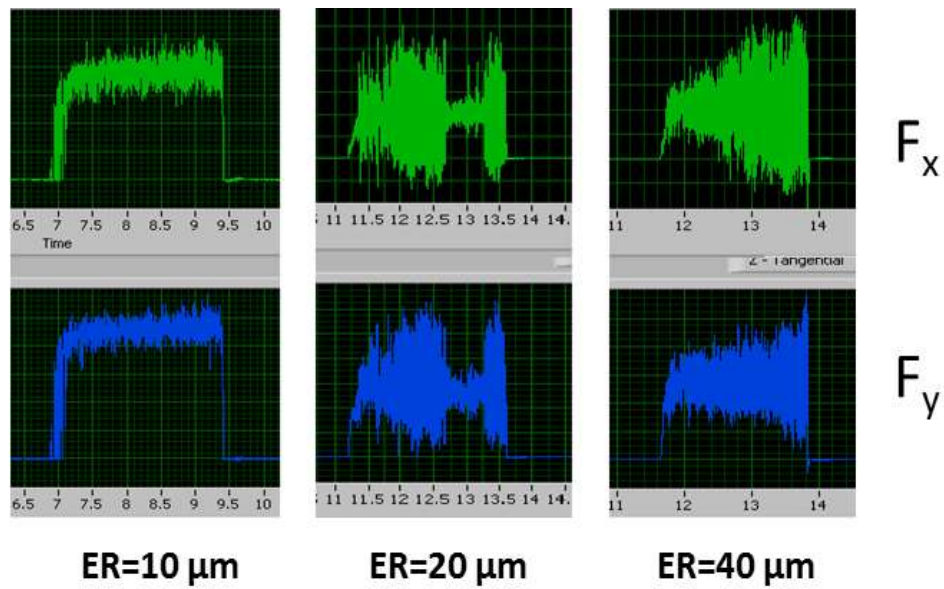


Fig 60) force spikes for feed = 0.05 (mm/rev)

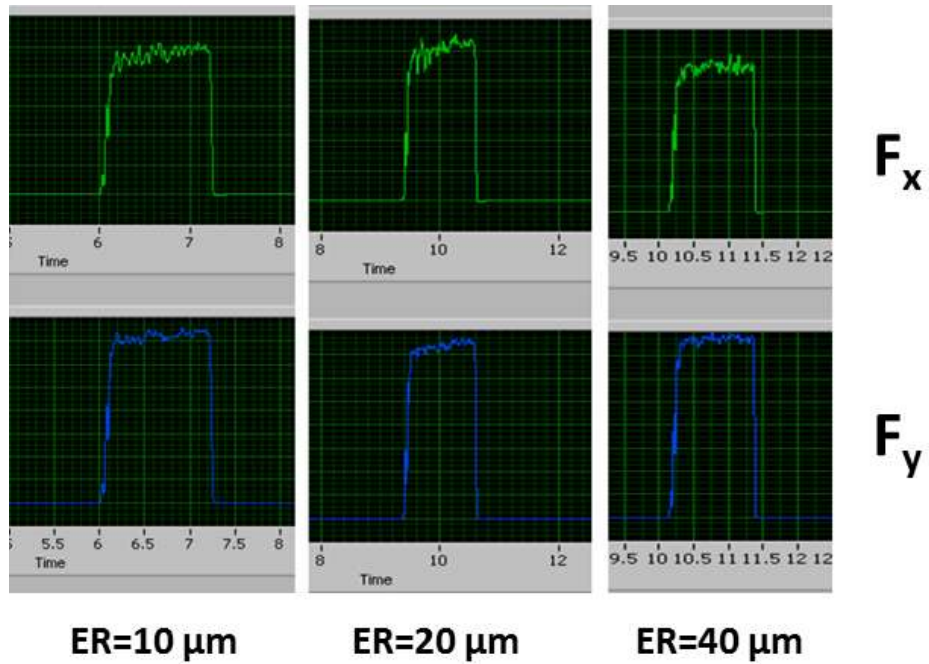


Fig 61) force spikes for feed=0.1(mm/rev)

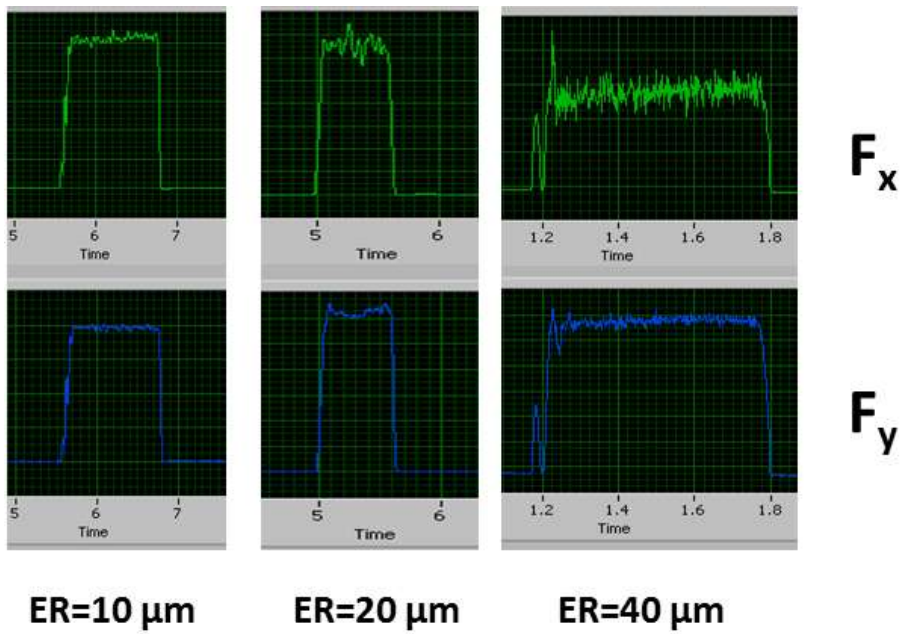
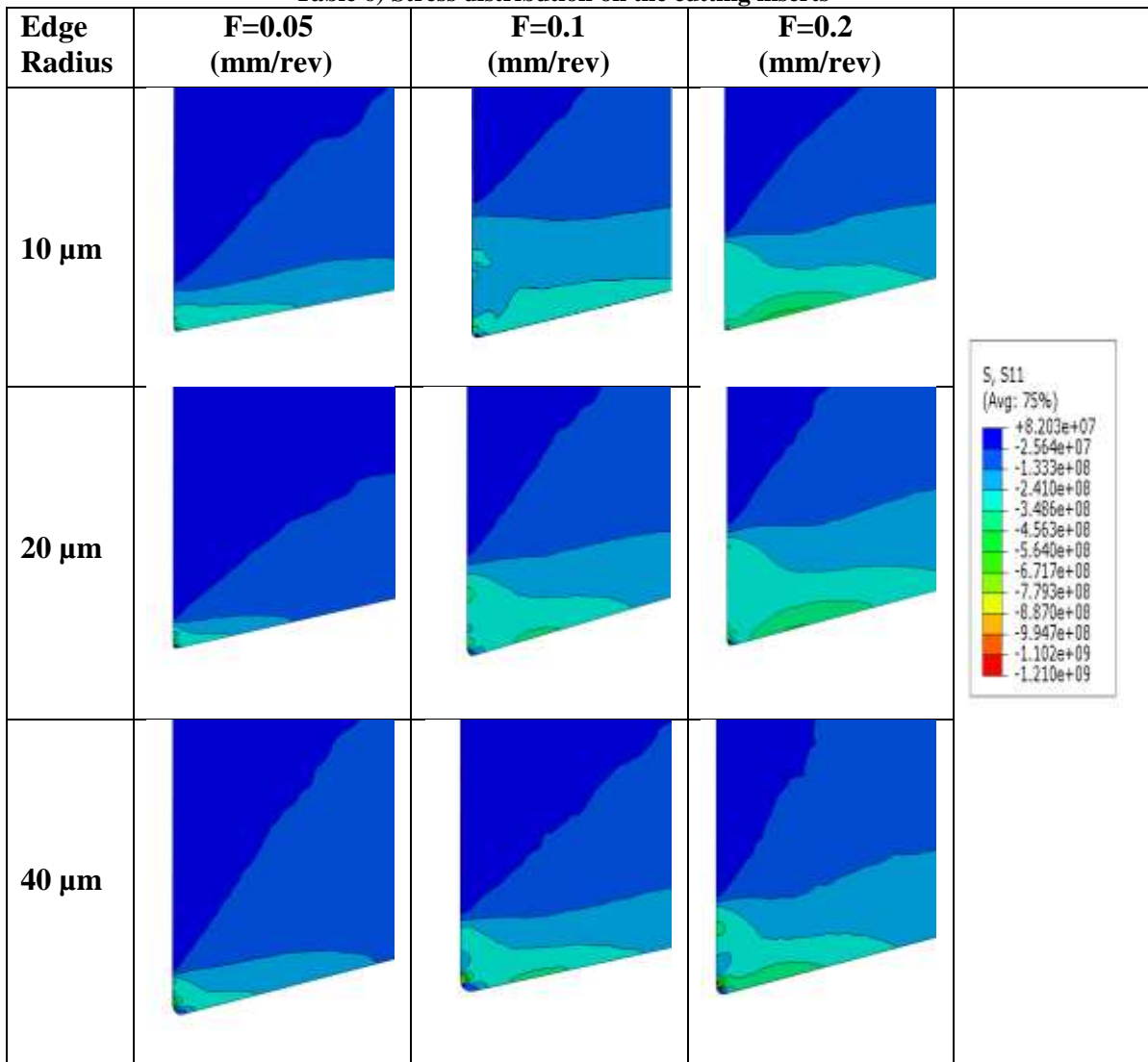


Fig 62) force spike for feed=0.2(mm/rev)

This also can be obtained from principal stress (S_{11}) contours on the tool face. By increasing the cutting feed, for all sets of edge radius the stress level increases on the flank face. This could be one reason for a shorter tool life (higher flank wear) at the higher cutting feed as outlined in Table 6.

Table 6) Stress distribution on the cutting inserts



5.2 Cutting forces

The two primary forces commonly considered in the metal cutting process are: tangential forces (cutting forces) normally resist the cutting motion and are responsible for removing material in the form of chips from the workpiece and thrust forces (feed forces) which contribute to the cutting process and assist curling of the chip along the rake face of the tool. Depending on cutting conditions and also the rake angle, the ratio between cutting and feed forces varies. In our application cutting forces consume a large percentage of cutting power compared to feed forces. For example, having negative rake angle leads to larger cutting forces but also to larger feed forces as well, which leads to a smaller ratio of cutting forces and feed forces. By increasing the cutting feed rate both the cutting and feed forces increase. This is attributed to a larger chip thickness as a result of smaller shear angle. When the size of the uncut chip thickness (feed) is very low, the chance of experiencing a size effect issue is high. Size effect refers to the relative size of the uncut chip thickness to the edge radius of the tool where small amounts of material, which do not cut but rather squeeze around the tool and generate a plowing effect. This can happen in cases with small feed rates. This could get worse as the sharpness of the tool decreases (larger edge radius) as the ratio between tool edge radius to uncut chip thickness (cutting feed rate in this study) approaches unity. So data oscillation was more intense when the feed was 0.05 (mm/rev) and tool edge radius was 40 μm , as the uncut chip thickness and edge radius are pretty close and the chance of plowing is very high. This issue was also observed by [68], and the solution offered was to change the cutting conditions or tool geometry, specifically the edge radius and rake angle.

5.3 Force data analysis

In order to smooth the cutting force data from the FE model, the data was filtered and then curve fitted using the Least Squares Method. This filtration excluded unsteady values and those data points which were outside the 70 percent of the average from the rest of the data points. Various types of functions have been used for curve fitting, with a polynomial of the third degree representing the minimum sum of squares in this case. Thus, to be consistent, this function has been applied to all cutting force data.

$$y = ax^3 + bx^2 + cx + d \quad (47)$$

The target was to modify the coefficients (a, b, c and d) to minimize the resulting sum which can be done by an algorithm in Microsoft Excel called “Solver Parameter”. Fig 63, Fig 64 and Fig 65 represent cutting and feed forces for each cutting tool with different cutting feed rates applied and Table 7 shows the error of prediction in each of these conditions. It is evident that by increasing the cutting feed, both cutting and feed forces increase significantly and this agrees with the experiments as larger cutting feed means that larger plastic work needs to be done.

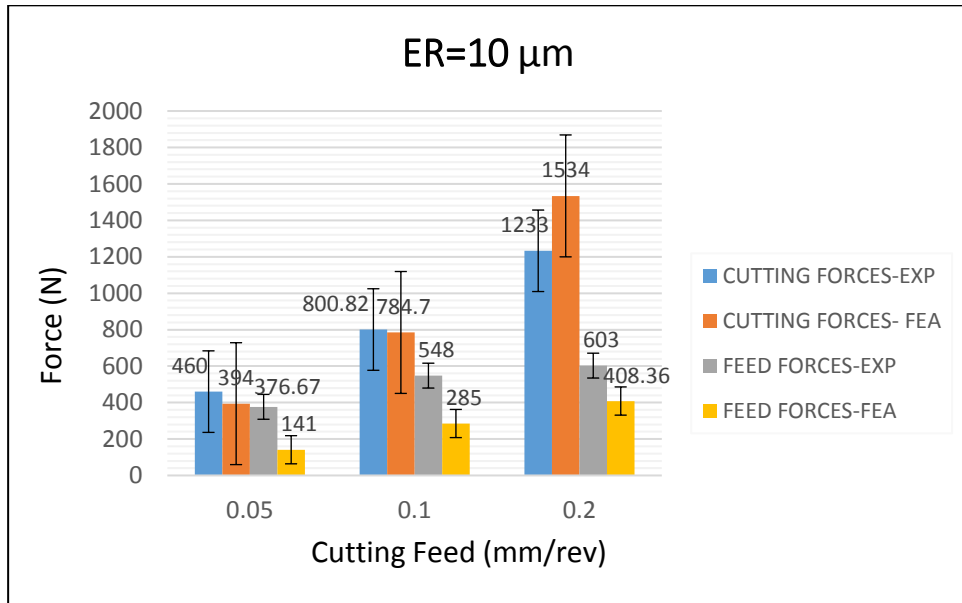


Fig 63) cutting force comparison for 10 μm corner radius

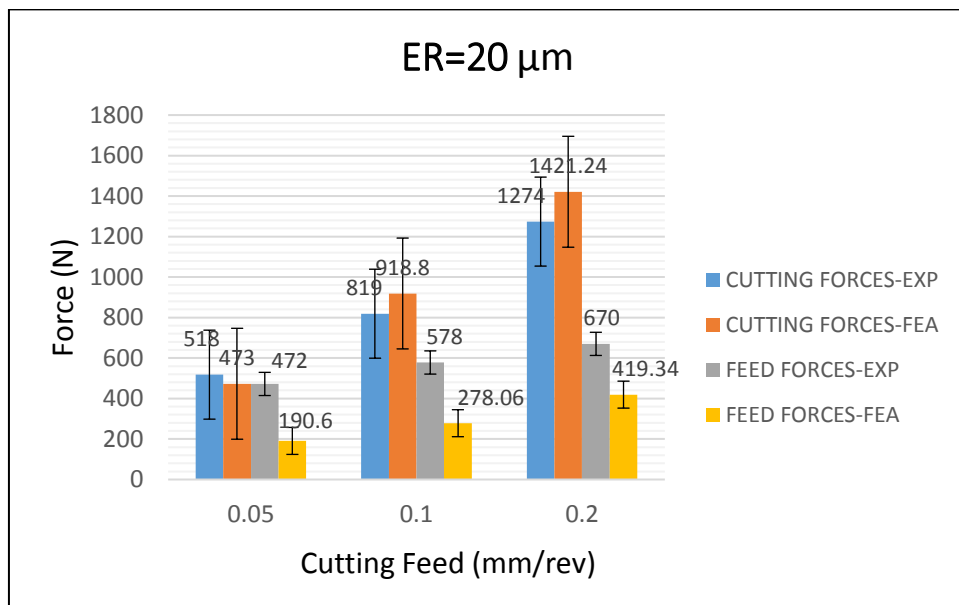


Fig 64) cutting force comparison for 20 μm corner radius

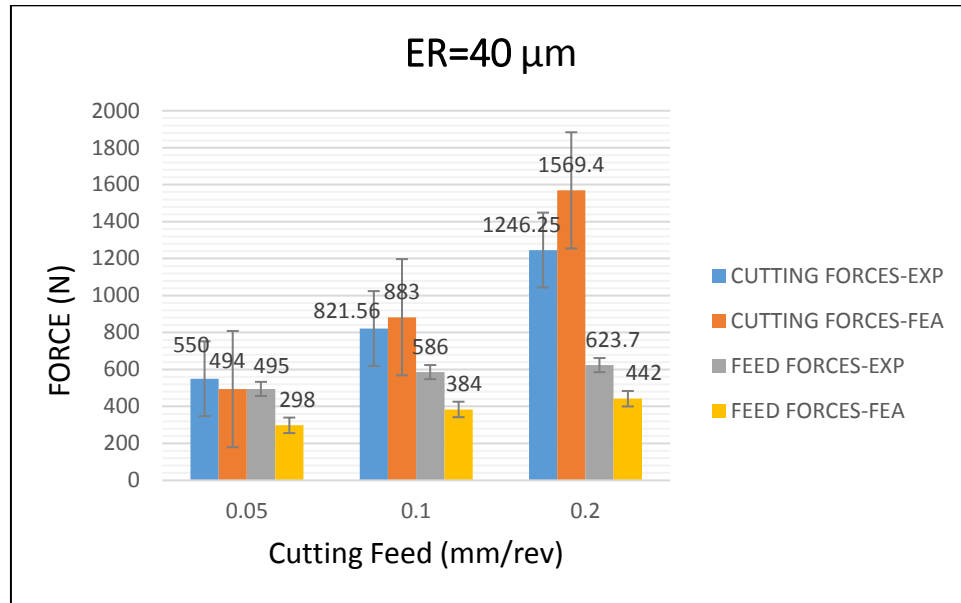


Fig 65) cutting force comparison for 40 μm corner radius

Table 7) Difference in prediction of cutting forces

	ER=10 μm		ER=20 μm		ER=40 μm	
F=0.05 (mm/rev)	14.34 %	62.5%	8.6%	59.6%	10.18%	39.79%
F=0.1 (mm/rev)	2.01%	48%	-12.18%	51.8%	-7.47%	34.47%
F=0.2 (mm/rev)	-24.4%	32.27%	-11.55%	37.4%	-25.92%	29.13%
	Cutting forces	Feed forces	Cutting forces	Feed forces	Cutting forces	Feed forces

From Table 7, it is evident that in all three cases, by increasing the cutting feed, the predicted feed forces align better with experimental data. This was likely due to the fact that when the material was sheared, the outer layers get strain hardened. Therefore, the hardness on the low cutting feed rate is larger than the material bulk hardness while by increasing the cutting feed, this parameter approaches the material bulk hardness. This effect is not considered in the model, so there is a larger difference at the low cutting feed rate. This trend was also observed by Hosseinkhani and Ng [48].

5.4 Temperature

For all cutting conditions, it was observed that the maximum temperature on the cutting tool occurs where the chip is about to totally be removed from the workpiece. Fig 66, Fig 67 and Fig 68 show the comparison between the highest temperatures for ($f=0.05$, $f=0.1$ and $f=0.2$) respectively at various edge radius values. Interestingly, these graphs were able to predict the same trend of Fig 59, which means that at the lowest cutting feed rate, the smallest edge radius had the highest temperature which leads to a lower tool life as compared to 0.1mm/rev . Also, by increasing the cutting feed rate an increase in temperature was observable. It also can be seen, except for the smallest cutting feed rate, that the tool with the largest edge radius had a higher maximum temperature. There is a plateau at the peak of each graph and also there is a tangible difference between the different cutting feed rates. Also when increasing the cutting feed rate, this line gets larger. This was likely due to the contact area and the area of highest temperature shifts more onto the rake face of the tool. Also at the same cutting feed, increasing the cutting edge radius, leads to a higher temperature except for minimum cutting feed rate, since the larger edge radius results in larger plastic work which plays an important role in temperature rise. This phenomenon did not occur at the minimum cutting feed rate due to the size effect which was discussed earlier.

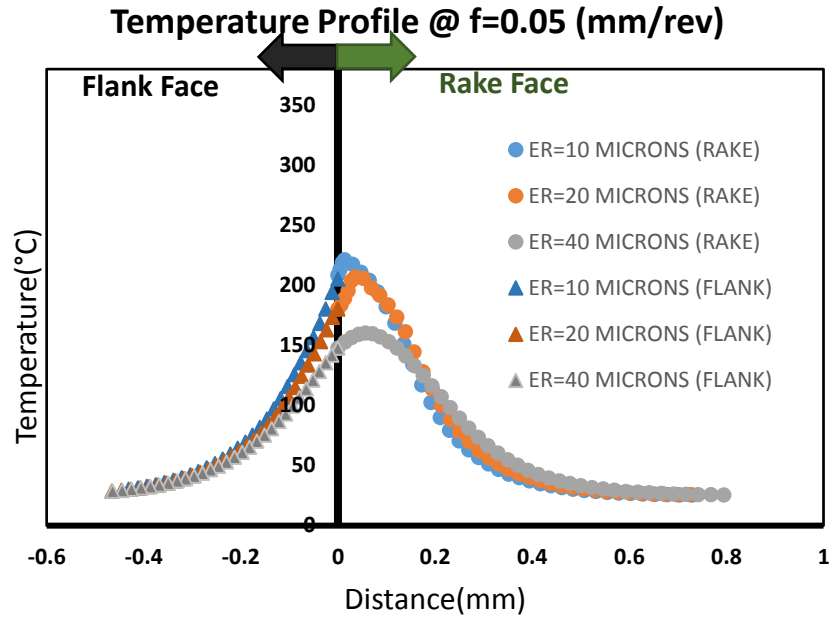


Fig 66) The temperature distribution along $f=0.05$ (mm/rev)

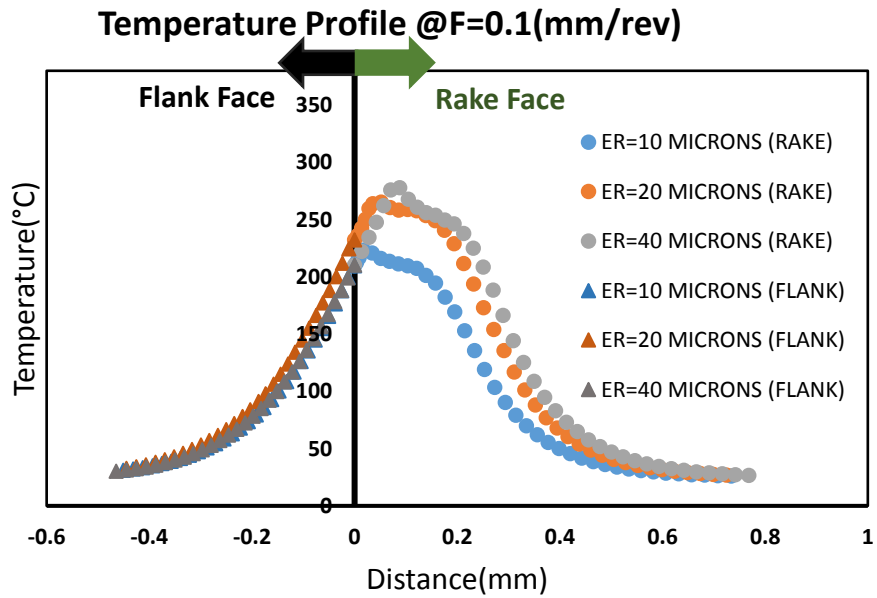


Fig 67) The temperature distribution along $f=0.1$ (mm/rev)

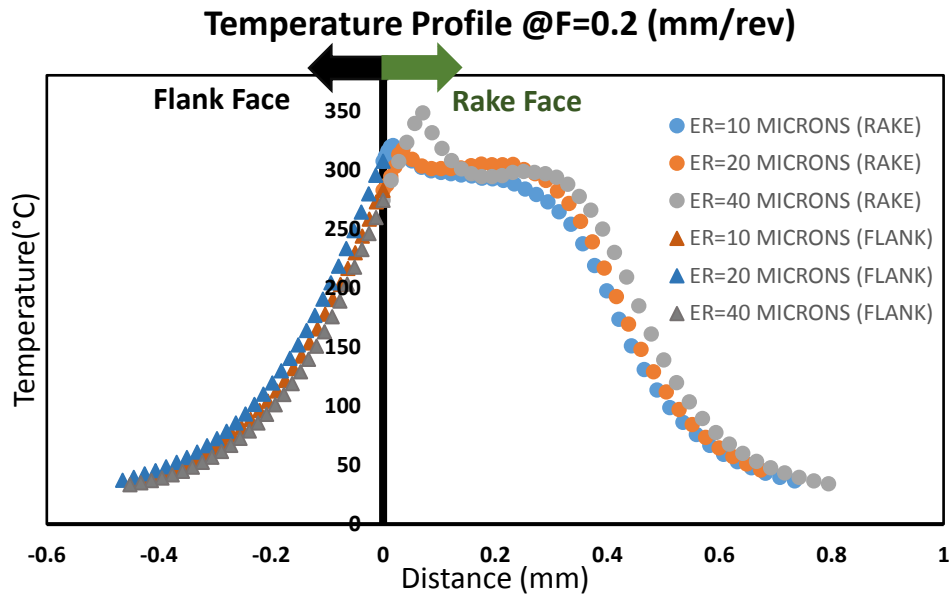


Fig 68) the temperature distribution along $f=0.2$ (mm/rev)

Also, by looking at the location of the maximum temperature for each cutting condition, it is evident that initially the location of maximum temperature starts from the tool tip, then it moves up along the rake face as the tool chip contact increases then it suddenly moves down and is located close to the tool tip. The explanation for this lies in the fact that when the chip starts to form, the tool chip contact area is not stabilized yet, so the maximum temperature is close to the tool tip, then because of crater wear on the rake face, the maximum temperature occurs at the maximum depth of crater wear. Finally, this location is located close to the tool tip as the tool wear starts at the cutting edge. Fig 70, Fig 71 and Fig 72 show the location of maximum temperature along the cutting edge to the rake face with different cutting feed at cutting edge radius of 10, 20 and 40 μm respectively. The reference point is located at the lowest point of the cutting edge where the rake face and flank face separate, Fig 69. By comparing these graphs, it can be understood that by

increasing the cutting feed rate the location of maximum temperature gets farther away from the tool tip, furthermore, as the cutting feed increases the return of maximum temperature close to the tool tip will be delayed. By comparing these three cutting edge radius, the 40 μm maximum temperature was close to the cutting edge for all the cutting conditions. This conclusion can clarify why 40 μm cutting tool edge radius has the shortest tool life.

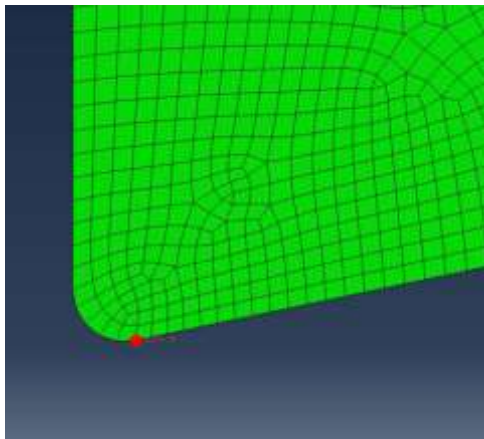


Fig 69) Tool reference

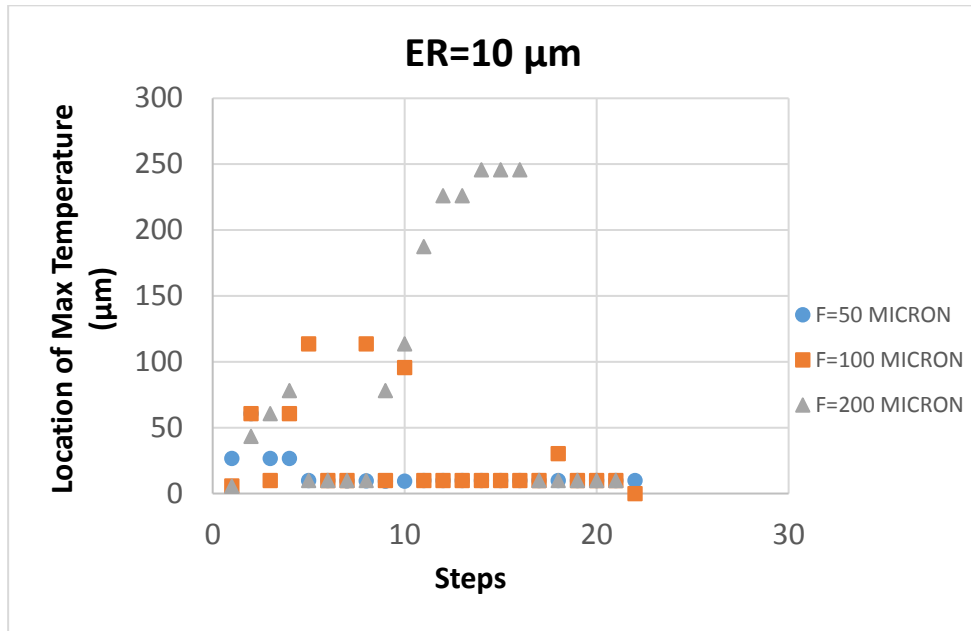


Fig 70) The location of maximum temperature at 10 μm cutting tool

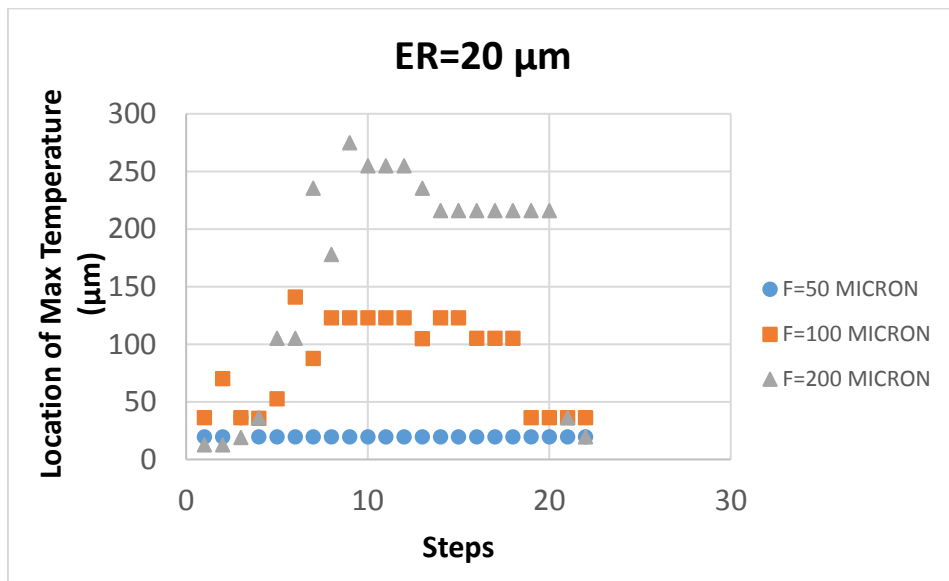


Fig 71) The location of maximum temperature at 20 μm cutting tool

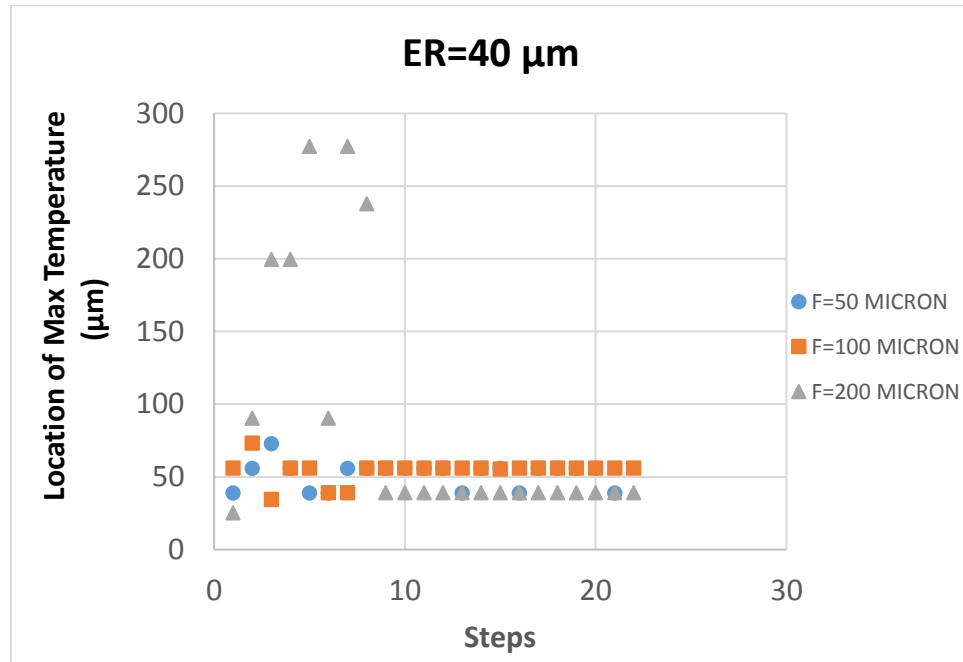


Fig 72) The location of maximum temperature at 40 μm cutting tool

This also can be visible by looking at the tool profile captured by the Alicona, after crater wear. As shown in Fig 73. By increasing the edge radius with similar feed, it was observed the maximum depth of crater wear, which corresponds to the highest temperature on the rake face due to a high temperatures ability to accelerate diffusion, becomes closer to the tool tip.

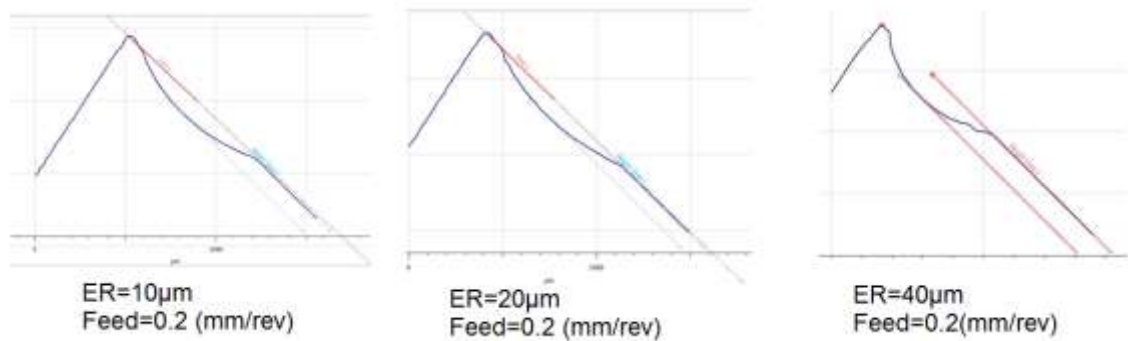


Fig 73) Distance from maximum depth of crater wear

Fig 74 shows the 20 μm tool profile where maximum crater wear occurs for various cutting feed rates, increasing the cutting feed rate the area of crater wear become larger and more spread out.

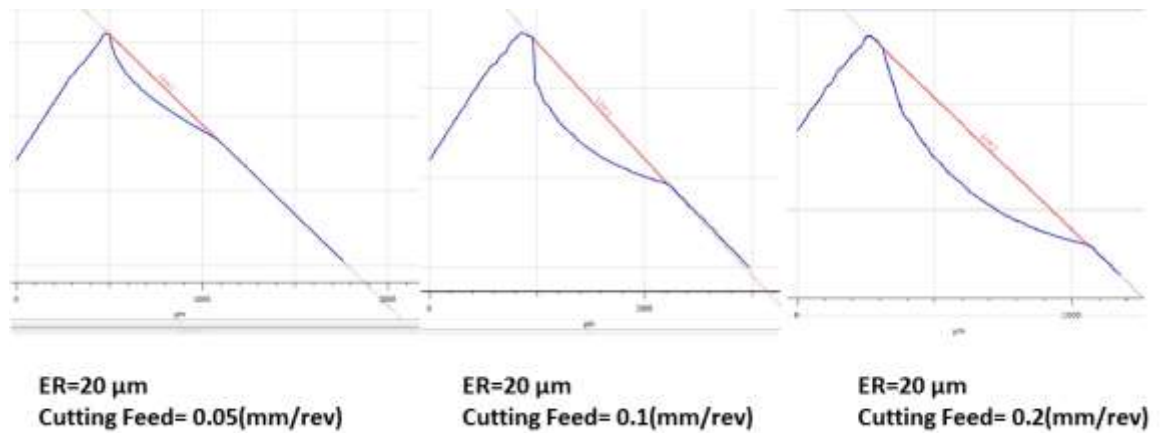

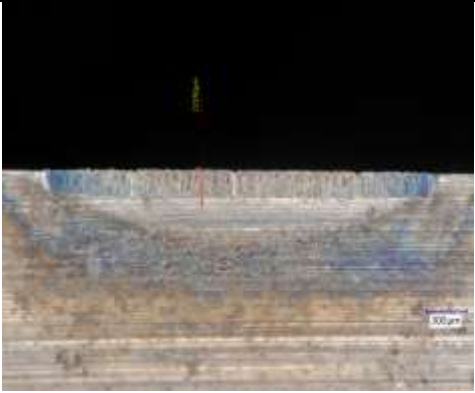



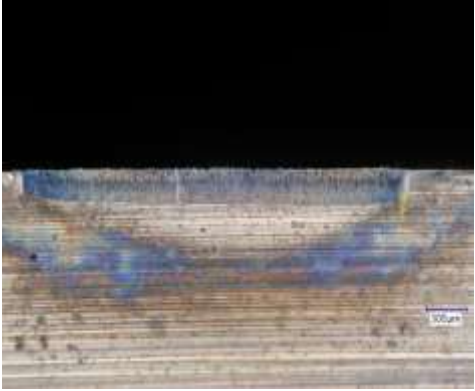


Fig 74) Increasing cutting feed-larger crater wear

Although smaller edge radiuses showed smaller flank wear, larger tool crater wear can be observed in some cases due to larger tool-chip contact area compared to other edge radiuses. As shown in Table 8.

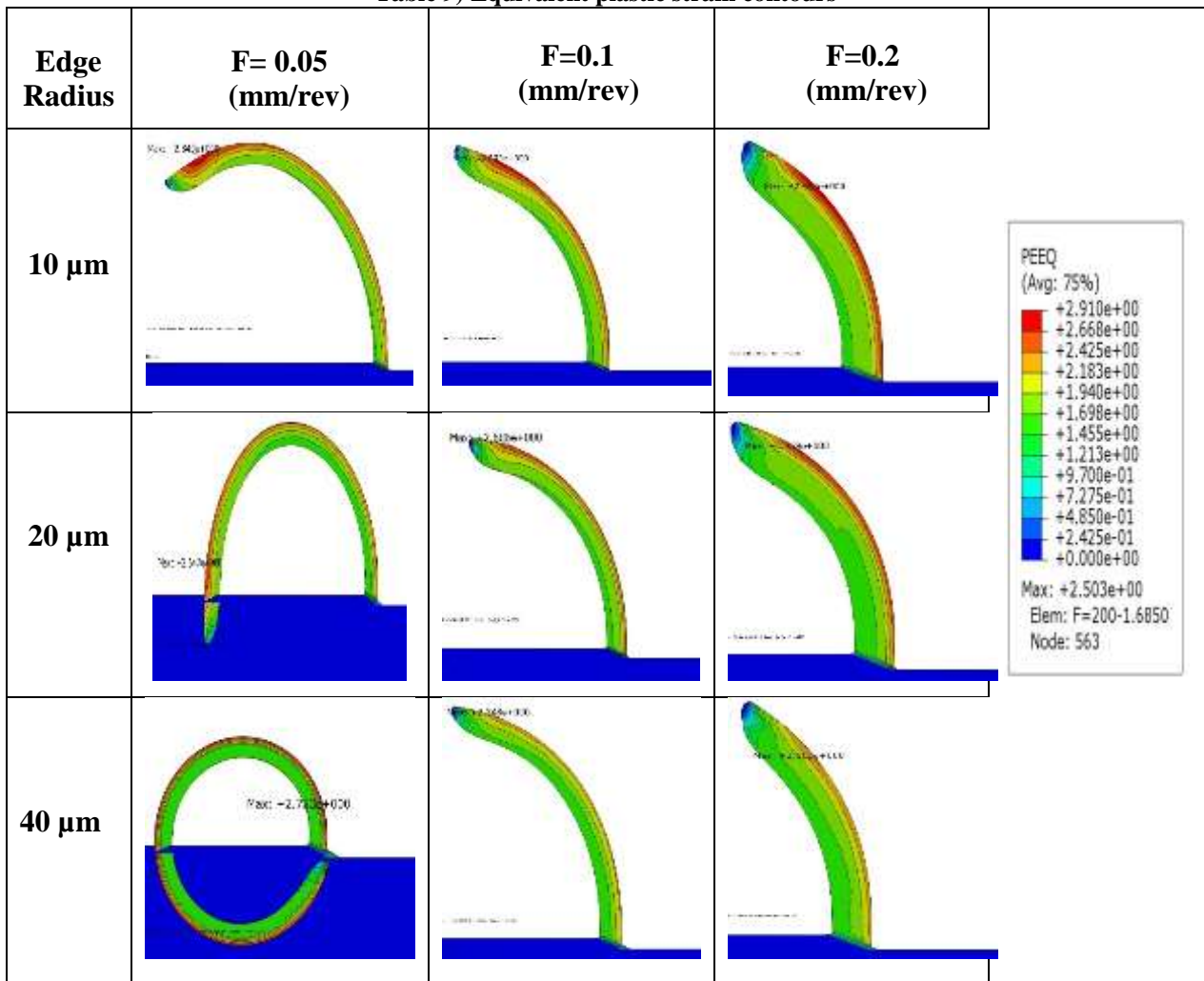
Table 8) Flank wear vs. Crater wear at constant feed for different edge radius (scale bar = 300 μm)

Edge Radius	Crater wear	Flank wear
10 μm		
20 μm		
40 μm		

5.5 Equivalent Plastic Strain (PEEQ)

As Shaw [8] mentioned, as the shear angle increases the chip thickness decreases and in turn the plastic strain in the chip decreases as well. So it is reasonable that by increasing the cutting feed rate, the value of equivalent plastic strain increases due to a larger chip thickness. As can be seen in Table 9, where PEEQ has been captured from a similar time step in each model, the maximum value showed a slight increase with higher cutting feed, while the area of higher equivalent plastic strain has increased substantially. It was also observed that by increasing edge radius the area of highest plastic strain becomes smaller and this is due to a smaller chip thickness at a higher edge radii and in turn this leads to lower plastic strain as discussed above except when edge radius was 40 μm and $f=0.05$ mm/rev. In this cutting condition, as mentioned before, the chance of plowing is larger than the other cutting conditions. It is known that the reason for a high level of plastic strain values compared to other operations relates to the intensity of normal stresses in the PSDZ. When these values are very high they retard the material separation from the workpiece. Since this is the case in this cutting condition, the effective rake angle is more negative so there is a possibility to increase the normal stresses and increase the level of plastic strain.

Table 9) Equivalent plastic strain contours



6. Conclusions

In this study, the performance of three different sets of edge radius were simulated using FEA and compared to experimental performance. This project used the Johnson-Cook damage parameters, imported from [58] which were established using tensile tests and were used to calibrate the damage parameters. The updated Lagrangian finite element models developed through ABAQUS/EXPLICIT with a set sacrificial layer dedicated to each tool

edge radius. Using this model cutting forces, feed forces and temperature and other required parameters to evaluate the tool performance were extracted. Orthogonal cutting through a plunging test was done under nine different feed rates but a constant cutting velocity. The cutting forces were collected and showed intense vibration at a low cutting feed rate which could be attributed to the light depth of cut at the lower feed rates. The predicted forces from FEA showed good agreement with experiments while, the feed force prediction, especially at the lower feed forces and small edge radius were high, and as mentioned this could be due to a higher material hardness at the outer layers of the workpiece which is the case in the low cutting feed case which is consistent with a similar trend described by Mohamad Nasr [69]. Also the sharpest tool at the middle feed rate showed the best tool life in this type of operation (plunging). This is due to the more favourable temperature distribution across the larger edge radii and also the lower temperature and stress concentration at the tool tip. Further, by increasing the cutting feed the stress distribution moves from the flank face to the rake face as the larger contact area is formed. In this experiment, increasing the cutting feed rate had an adverse effect on both the crater wear and flank wear. The main reason for flank wear was the higher stress on the flank face and the temperature rise under the higher cutting feed rate which led to more aggressive crater wear on the rake face.

7. Recommendations for Future Work

The updated Lagrangian model has been used for material deformation in metal cutting, through ABAQUS/CAE associated with tangential behavior contact between the tool and

the workpiece. Constant value of friction has been based on literature and this assumption was fair as the cutting process was short and process was not exposed to elevated temperatures. However, as mentioned in the chapter “Friction in Machining”, in metal cutting as the tool chip contact approximates to the sticking zone under high normal stresses. In other words, the correlation between shear and normal stress is not linear any more. Thus, the following suggestions are outlined as future work:

- 1- In future studies additional research could go into tuning the coefficient of friction to be closer to the conditions experienced in the cutting zone. This could help to alleviate the mismatch between experimental and numerical results.
- 2- Consider various sets of edge radiuses and cutting conditions for the plunging operation and also for the turning operation.
- 3- It was shown that sharper tools are more prone to crater wear while they are more resistant to flank wear. This can introduce a research opportunity to find the optimized edge radius that shows minimum wear both on the rake face and flank face.

8. References

- [1] B. E. Klamecki, "Incipient Chip Formation in Metal Cutting--a Three-dimension Finite Element Analysis", University of Illinois at Urbana-Champaign, 1973.
- [2] E. Usui and T. Shirakashi, "Mechanics of machining—from descriptive to predictive theory", *On the Art of Cutting Metal 75 Years Later*, vol. 7, pp. 13–35, 1982.
- [3] K. Iwata, K. Osakada, and Y. Terasaka, "Process modeling of orthogonal cutting by the rigid-plastic finite element method", *J. Eng. Mater. Technol.*, vol. 106, no. 2, pp. 132–138, 1984.
- [4] J. S. Strenkowski and J. T. Carroll, "A finite element model of orthogonal metal cutting", *J. Eng. Ind.*, vol. 107, no. 4, pp. 349–354, 1985.
- [5] L. Olovsson, L. Nilsson, and K. Simonsson, "An ALE formulation for the solution of two-dimensional metal cutting problems", *Computers & Structures*, vol. 72, no. 4, pp. 497–507, 1999.
- [6] T. Özel, T.K. Hsu, and E. Zeren, "Effects of cutting edge geometry , workpiece hardness , feed rate and cutting speed on surface roughness and forces in finish turning of hardened AISI H13 steel", *The International Journal of Advanced Manufacturing Technology*, vol. 25, no. 3, pp. 262–269, 2005.
- [7] P. J. Ñ. Arrazola, D. Ugarte, and X. Dominguez, "A new approach for the friction identification during machining through the use of finite element modeling", *International Journal of Machine Tools and Manufacture*, vol. 48, no. 2, pp. 173–183, 2008.

- [8] M. C. Shaw, *Metal Cutting Principles*, 2nd ed., Oxford University Press, 2004.
- [9] M. E. Merchant, "Mechanics of the metal cutting process. I. Orthogonal cutting and a type 2 chip", *J. Appl. Phys.*, vol. 16, no. 5, pp. 267–275, 1945.
- [10] K. Nakayama, "A study on chip-breaker", *Bulletin of JSME*. vol. 5, no. 17, pp. 142-150, 1962.
- [11] S. Y. Hong, Y. Ding, and R. G. Ekkens, "Improving low carbon steel chip breakability by cryogenic chip cooling", *International Journal of Machine Tools and Manufacture*, vol. 39, no. 7, pp. 1065–1085, 1999.
- [12] G. Boothroyd, "Fundamentals of Machining and Machine Tools", Taylor & Francis, 1975.
- [13] S. Zhang, J. Li, X. Zhu, and H. Lv, "Saw-Tooth Chip Formation and Its Effect on Cutting Force Fluctuation in Turning of Inconel 718", *International Journal of Precision Engineering and Manufacturing*, vol. 14, no. 6, pp.957–963, 2013.
- [14] A. Devotta, T. Beno, R. Siriki, R. Löf, and M. Eynian, "Finite element modeling and validation of chip segmentation in machining of AISI 1045 steel", *Procedia CIRP*, vol. 58, pp. 499–504, 2017.
- [15] G.G. Ye, S.F. Xue, W. Ma, M.Q. Jiang, Z. Ling, X.H. Tong, and L.H. Dai, "Cutting AISI 1045 steel at very high speeds", *International Journal of Machine Tools & Manufacture* vol. 56, pp. 1–9, 2012.
- [16] V. P. Astakhov, *Geometry of single-point turning tools and drills: fundamentals and practical applications*, Springer Science & Business Media, 2010.

- [17] N. A. Abukhshim, P. T. Mativenga, and M. A. Sheikh, "Heat generation and temperature prediction in metal cutting: A review and implications for high speed machining", *Int. J. Mach. Tools Manuf.*, vol. 46, no. 7–8, pp. 782–800, 2006.
- [18] V. P. Astakhov and S. Shvets, "The assessment of plastic deformation in metal cutting", *Journal of Materials Processing Technology* vol. 146, no. 2, pp. 193–202, 2004.
- [19] B. Denkena and D. Biermann, "Cutting edge geometries", *CIRP Annals*, vol. 63, pp. 631–653, 2014.
- [20] C. J. C., Rodriguez, "Cutting edge preparation of precision cutting tools by applying micro-abrasive jet machining and brushing", Kassel University Press, 2009.
- [21] E. Uhlmann, J. König, A. Dethlefs, and M. G. vd Schulenburg, "Charakterisierung geometrisch bestimmter Schneiden; neue Kennwerte zur Charakterisierung von Schneidkanten an strömungsgeschliffenen Wendeschneidplatten", *wt Werkstattstech. online*, vol. H, vol. 7, no. 8, pp. 475–481, 2011.
- [22] M. R. Movahhedy, Y. Altintas, and M. S. Gadala, "Numerical Analysis of metal Cutting With Chamfered and Blunt Tools", *J. Manuf. Sci. Eng.* vol. 124, no.4, pp. 178-188, 2002.
- [23] H. Ren and Y. Altintas, "Mechanics of Machining With Chamfered Tools", *Transactions of ASME*, vol. 122, no.4 pp. 650-659, 2000.
- [24] Y. C. Yen, A. Jain, and T. Altan, "A finite element analysis of orthogonal machining using different tool edge geometries", *J. Mater. Process. Technol.*, vol. 146, no. 1, pp. 72–81, 2004.

- [25] M. N. A. Nasr, E. G. Ng, and M. A. Elbestawi, "Modelling the effects of tool-edge radius on residual stresses when orthogonal cutting AISI 316L", *Int. J. Mach. Tools Manuf.*, vol. 47, no. 2, pp. 401–411, 2007.
- [26] T. Özel and E. Zeren, "Finite element modeling the influence of edge roundness on the stress and temperature fields induced by high-speed machining", *Int. J. Adv. Manuf. Technol.*, vol. 35, no. 3–4, pp. 255–267, 2007.
- [27] I. Al-Zkeri, J. Rech, T. Altan, H. Hamdi, and F. Valiorgue, "Optimization of the Cutting Edge Geometry of Coated Carbide Tools in Dry Turning of Steels Using a Finite Element Analysis", *Mach. Sci. Technol.*, vol. 13, no. 1, pp. 36–51, 2009.
- [28] J. Fulemova and Z. Janda, "Influence of the Cutting Edge Radius and the Cutting Edge Preparation on Tool Life and Cutting Forces at Inserts with Wiper Geometry", *Procedia Eng.*, vol. 69, pp. 565–573, 2014.
- [29] S. Subbiah and S. N. Melkote, "Effect of finite edge radius on ductile fracture ahead of the cutting tool edge in micro-cutting of Al2024-T3", *Mater. Sci. Eng. A*, vol. 474, no. 1–2, pp. 283–300, 2008.
- [30] Y. Karpaz, *Predictive modeling and optimization in hard turning: investigations of effects on cutting tool micro-geometry*, Rutgers The State University of New Jersey-New Brunswick, 2007.
- [31] Y. Karpaz and A. Srivastava, "Hard turning with variable micro-geometry PcBN tools", *CIRP Annals*, vol. 57, pp. 73–76, 2008.

- [32] J. T. Burwell, and C. D. Strang, "On the Empirical Law of Adhesive Wear", *Journal of Applied Physics*, vol. 23, no. 1, pp. 18-28, 1952.
- [33] B. Li, "A review of tool wear estimation using theoretical analysis and numerical simulation technologies", *Int. J. Refract. Met. Hard Mater.*, vol. 35, pp. 143–151, 2012.
- [34] U. Khandey, "Optimization of surface roughness, material removal rate and cutting tool flank wear in turning using extended Taguchi approach", *Doctoral Dissertation*, 2009.
- [35] Y. N. Zarif, "Cutting Edge Microgeometry, Modeling and EE-Honing", *McMaster University PhD Dissertation*, 2012.
- [36] K. Bouzakis, N. Michailidis, G. Skordaris, E. Bouzakis, D. Biermann, and R. M. Saoubi, "Cutting with coated tools : Coating technologies , characterization methods and performance optimization", *CIRP Ann. - Manuf. Technol.*, vol. 61, no. 2, pp. 703–723, 2012.
- [37] J. Rech, "Influence of cutting tool coatings on the tribological phenomena at the tool – chip interface in orthogonal dry turning the tool – chip interface in orthogonal dry turning", *Surface coatings and Technology*, vol. 200. no.16, pp. 5132-5139, 2006.
- [38] J. P. Davim, editor, *Tribology in Manufacturing Technology*, Springer Science & Business Media, 2012.
- [39] L. Ning, "Nano-multilayered Self-adaptive Hard PVD Coatings for Dry High Performance Machining", *McMaster Ph.D. Dissertation*, 2014.

- [40] S. Atlati, B. Haddag, M. Nouari, and M. Zenasni, "Thermomechanical modelling of the tool-workmaterial interface in machining and its implementation using the ABAQUS VUINTER subroutine", *Int. J. Mech. Sci.*, vol. 87, pp. 102–117, 2014.
- [41] D. Ulutan and T. Ozel, "Machining induced surface integrity in titanium and nickel alloys: A review", *Int. J. Mach. Tools Manuf.*, vol. 51, no. 3, pp. 250–280, 2011.
- [42] M. Guediche, T. Mabrouki, C. Donnet, J. M. Bergheau, and H. Hamdi, "A new procedure to increase the orthogonal cutting machining time simulated", *Procedia CIRP*, vol. 31, pp. 299–303, 2015.
- [43] J. Ma, N. H. Duong, S. Chang, Y. Lian, J. Deng, and S. Lei, "Assessment of Microgrooved Cutting Tool in Dry Machining of AISI 1045 Steel", *J. Manuf. Sci. Eng.*, vol. 137, no. 3, pp. 1–9, 2015.
- [44] C. Courbon, T. Mabrouki, J. Rech, D. Mazuyer, and E. D'Eramo, "On the existence of a thermal contact resistance at the tool-chip interface in dry cutting of AISI 1045: Formation mechanisms and influence on the cutting process", *Appl. Therm. Eng.*, vol. 50, no. 1, pp. 1311–1325, 2013.
- [45] H. Ding and Y. C. Shin, "A Metallo-Thermomechanically Coupled Analysis of Orthogonal Cutting of AISI 1045 Steel", *J. Manuf. Sci. Eng.*, vol. 134, no. 5, p. 51014, 2012.
- [46] Y. Xi, M. Bermingham, G. Wang, and M. Dargusch, "FEA Modelling of Cutting Force and Chip Formation in Thermally Assisted Machining of Ti6Al4V Alloy", *Mater. Sci. Forum*, vol. 765, pp. 343–347, 2013.

- [47] M. Calamaz, D. Coupard, and F. Girot, "A new material model for 2D numerical simulation of serrated chip formation when machining titanium alloy Ti-6Al-4V", *Int. J. Mach. Tools Manuf.*, vol. 48, no. 3–4, pp. 275–288, 2008.
- [48] K. Hosseinkhani and E. Ng, "Analysis of the cutting mechanics under the influence of worn tool geometry", *Procedia CIRP*, vol. 8, pp. 117–122, 2013.
- [49] Y. Bao and T. Wierzbicki, "A Comparative Study on Various Ductile Crack Formation Criteria", *J. Eng. Mater. Technol.*, vol. 126, no. 3, pp. 314, 2004.
- [50] J. Liu, Y. Bai, and C. Xu, "Evaluation of Ductile Fracture Models in Finite Element Simulation of Metal Cutting Processes", *J. Manuf. Sci. Eng.*, vol. 136, no. 1, p. 11010, 2014.
- [51] Y. Bao and T. Wierzbicki, "On fracture locus in the equivalent strain and stress triaxiality space", *International Journal of Mechanical Sciences*, vol. 46, no. 1, pp. 81–98, 2004.
- [52] Y. Zhang, J. C. Outeiro, and T. Mabrouki, "On the selection of Johnson-Cook constitutive model parameters for Ti-6Al-4V using three types of numerical models of orthogonal cutting", *Procedia CIRP*, vol. 31, pp. 112–117, 2015.
- [53] X. Teng, T. Wierzbicki, S. Hiermaier, I. Rohr, "Numerical prediction of fracture in the Taylor Test", *International Journal of Solids and Structures*, vol. 42, no. 9, pp. 2929–2948, 2005.
- [54] J. T. Carroll and J. S. Strenkowski, "Finite Element Models of Orthogonal Cutting With Application to Single Point Diamond Turning", *International Journal of Mechanical Sciences*, vol. 30, no. 12, pp. 899–920, 1988.

- [55] Z. C. Lin and S. Y. Lin, "A coupled finite element model of thermo-elastic-plastic large deformation for orthogonal cutting", *ASME J. Eng. Ind.*, vol. 114, pp. 218–226, 1992.
- [56] E. Ceretti, P. Fallböhmer, W. T. Wu, and T. Altan, "Application of 2D FEM to chip formation in orthogonal cutting", *J. Mater. Process. Technol.*, vol. 59, no. 1–2, pp. 169–180, 1996.
- [57] B. Zhang and A. Bagchi, "Finite element simulation of chip formation and comparison with machining experiment", *J. Eng. Ind.*, vol. 116, no. 3, pp. 289–297, 1994.
- [58] K. Wang, "Calibration of the Johnson-Cook Failure Parameters as the Chip Separation Criterion in the Modelling of the Orthogonal Metal Cutting Process", McMaster Ph.D. Dissertation, 2016.
- [59] M. Zetterberg, "A critical overview of machining simulations in ABAQUS", (2014).
- [60] S. R. Idelsohn, E. Oñate, and F. Del Pin, "The particle finite element method : a powerful tool to solve incompressible flows with free-surfaces and breaking waves", *International Journal for Numerical Methods in Engineering*, vol. 61, no. 7, pp. 964–989, 2004.
- [61] J. P. Davim, editor, *Machining: Fundamentals and Recent Advances*, Springer Science & Business Media, 2008.
- [62] C. Kiliçaslan, "Modelling and Simulation of Metal Cutting by Finite Element Method", M.S. Thesis, Izmi Institute of Technology, 2009.
- [63] Dassault Systèmes Simulia, "Abaqus 6.14 CAE User Guide", p. 1146, 2014.

- [64] S. P. F. C. Jaspers and J. H. Dautzenberg, "Material behaviour in conditions similar to metal cutting: Flow stress in the primary shear zone", *J. Mater. Process. Technol.*, vol. 122, no. 2–3, pp. 322–330, 2002.
- [65] J., Borkevec and J. Petruska, "Computer Simulation of Material Separation Process", *Proc. Engineering Mechanics, Svratka, Czech Republic*, 2007.
- [66] G. Johnson and W. H. Cook, "Fracture Characteristics of Three Metals Subjected to Various Strains, Strain Rates, Temperatures and Pressures", *Engineering Fracture Mechanics*, vol. 21, no. 1, pp. 31-48, 1985.
- [67] V. P. Astakhov, "Effects of the cutting feed , depth of cut , and workpiece (bore) diameter on the tool wear rate", *International Journal of Advanced Manufacturing Technology*, vol. 34, no. 7, pp. 631-640, 2007.
- [68] A. Shrot and M. Bäker, "Determination of Johnson – Cook parameters from machining simulations", *Comput. Mater. Sci.*, vol. 52, no. 1, pp. 298–304, 2012.
- [69] M. N. A. Nasr, "Effects of Sequential Cuts on Residual Stresses when Orthogonal Cutting", *Procedia CIRP*, vol. 31, pp. 118–123, 2015.